Power Decoupling Method for Voltage Source Inverters Using Grid Voltage Modulated Direct Power Control in Unbalanced System

Gong, Zhen; Liu, Chengxi; Gui, Yonghao; Silva, Filipe Miguel Faria da; Bak, Claus Leth

Published in:
IEEE Transactions on Power Electronics

Publication date:
2022

Power Decoupling Method for Voltage Source Inverters Using Grid Voltage Modulated Direct Power Control in Unbalanced System

Zhen Gong, *Student Member, IEEE*, Chengxi Liu, *Senior Member, IEEE*, Yonghao Gui, *Senior Member, IEEE*, Filipe Faria da Silva, *Senior Member, IEEE*, Claus Leth Bak, *Senior Member*, *IEEE*

***Abstract*—The grid voltage modulated direct power control (GVM-DPC) is a novel power regulation method for grid-connected voltage source inverters (VSI). However, interactions between real and reactive powers still exist in GVM-DPC under unbalanced grid voltage condition, which may deteriorate its transient performance. This paper proposes a power decoupling method for GVM-DPC-based VSI in unbalanced systems based on the dynamic feedforward power compensation (DFPC) strategy, which can reduce the coupling magnitudes of real and reactive powers in the transient stages. Firstly, the power coupling mechanism of positive and negative sequence real and reactive powers of VSI under the unbalanced voltage condition is analyzed. Then, the power coupling magnitudes (PCM) are derived according to relationships among the positive sequence components of real power, reactive power and PCC voltages. Next, the PCM are compensated into the GVM-DPC for the better decoupling performance. Furthermore, a stability analysis of the proposed control system is studied based on the impedance model, and a comparison with the traditional power decoupling method based on virtual impedance is conducted to show the superiority of the proposed method. Finally, simulations, hardware-in-loop test and experiment are conducted to validate the effectiveness of the proposed method.**

***Index Terms*—grid-voltage-modulated direct power control, power decoupling, voltage source inverter, unbalanced system.**

I. Introduction

With the installation of renewable generations, voltage source inverter (VSI) is usually utilized to integrate them into the power grids [1]. Different control strategies have been proposed to improve the VSI reliability, efficiency and safety [2]-[7]. Among them, the direct power control (DPC) is proposed for VSI to regulate output real and reactive powers directly without using phase-locked loop (PLL), which can achieve better dynamic performance and robustness comparing with conventional vector-oriented controls (VOC) [8]-[10].

Inspired by the direct torque control, a look-up-table DPC (LUT-DPC) is investigated which dynamic performance is proved to be faster than VOC [9]. However, the switching frequency is a time-varying value, which will result in the undesirable broadband harmonic fluctuations in output powers. To tackle this issue, different DPC methods are explored [11]-[19]. For example, a sliding-mode-control-based DPC is proposed to realize the constant switching frequency and robustness [11], [12]. Nevertheless, large ripples in output powers still exists and the convergence of its operation point cannot be guaranteed. Besides, a model predictive control DPC is proposed in [13], [14], which selects the optimal voltage vector to reduce the mutual interactions between the real and reactive powers based on the minimization of cost function. However, the evaluation of optimal voltage vector is time consuming. Recently, a novel grid voltage modulated-DPC (GVM-DPC) is proposed in [15]-[19], which makes the system a linear time-invariant system and solves the problems of large power harmonics induced by the nonlinear control characteristics of conventional DPC methods [15]. However, the coupling mechanism of real and reactive powers in the transient stages has not been given a full consideration under the unbalanced grid voltage condition, which may significantly degrade the dynamic performance and stability of low-inertia power systems [20], [21]. Thus, it is essential to develop power decoupling strategies to address the coupling problem suffered by the existing GVM-DPC in unbalanced system.

There are 4 types of power decoupling methods for VSI in distribution grids: 1) virtual power method (VPM) [22], 2) virtual frequency and voltage-based method (VFVM) [23], 3) virtual impedance method (VIM) [24]-[26], and 4) coupling compensation method (CCM) [31],[32]. The core ideas of VPM and VFVM are to rotate the vectors of real and reactive powers or vectors of voltage and frequency by an impedance angle. The VIM is to reshape the connecting line to be inductive by embedding virtual impedance into virtual synchronous generator control loop. The CCM adds coupling components of real and reactive powers into power control loops for the decoupling. However, all these power decoupling methods are designed for conventional virtual synchronous generator controls or droop controls, without considering the dynamic performance of GVM-DPC. Moreover, above methods only propose the power decoupling methods for VSI in 3-phase balanced system, without considering the power coupling mechanism under unbalanced voltage conditions.

This work was supported by the National Natural Science Foundation of China under Project 52007133 and Project U22B20100. (*Corresponding author: Chengxi Liu*)

Zhen Gong, Chengxi Liu are with the School of Electrical Engineering and Automation, Wuhan University, Wuhan 430072, China (email: gongzhen@whu.edu.cn; liuchengxi@whu.edu.cn). Zhen Gong is also with the Department of Energy Technology, Aalborg University, 9220 Aalborg, Demark.

Yonghao Gui is with the Electrification and Energy Infrastructures Division, Oak Ridge National Laboratory, USA (email: guiy@ornl.gov)

Filipe Faria da Silva, Claus Leth Bak are with the Department of Energy, Aalborg University, 9220 Aalborg, Demark (email: ffs@et.aau.dk; clb@et.aau.dk)

A parallel compensator (PC) is proposed for GVM-DPC under unbalanced grid voltage condition to improve the steady state performance [33]. In this case, output currents are balanced and real and reactive power ripples induced by negative current components are reduced. However, the GVM-DPC is based on an ideal grid condition, assuming that the voltage is not distorted by output powers of VSI, however, this assumption is not suitable for VSI connected to weak grids that the variation of voltage angle difference from PCC to grid side buses cannot be neglected, which will result in the severe power coupling issues. In [34]-[37], a new DPC method based on extended Akagi power theory is proposed, which can be directly used for VSI under balanced and unbalanced grid voltage conditions. It points out that traditional VSI control methods need to add power compensation values by extracting positive and negative sequence components to eliminate negative sequence components of output currents under unbalanced network condition. On the contrary, this sequence extraction is not required in the extended-power-theory-based DPC, which further simplifies the structure of the system. However, the real and reactive power coupling mechanism in transient stages is not considered in this method, since it also assumes that both positive and negative sequence voltages rotate with a fundamental angular frequency without considering the variation of angle difference between PCC voltage and grid voltage, which is not reasonable when VSI output powers change in the weak grid system. This assumption can lead to severer power coupling issues, which is the focus of this paper, and the conventional GVM-DPC method is selected as an example to clarify the contribution, revealing that the assumed ideal voltage condition in GVM-DPC will lead to power coupling phenomenon, which is also illustrated by phasor diagram of voltage and current. Then, the VSI powers can be decoupled by the proposed compensating power coupling magnitudes into the DPC loop, which can improve the power tracking performance.

Since there is no research focusing on the power coupling issues of GVM-DPC-based VSI under unbalanced voltage condition system, this paper proposes a power decoupling strategy for GVM-DPC under the unbalanced system based on the dynamic feedforward power compensation (DFPC) algorithm. The main contributions are summarized as follows:

1) The physical essences of power coupling in positive and negative sequence are visualized by phasor diagrams.

2) The limited power decoupling capability of existing GVM-DPC under unbalanced system is pointed out by mathematical derivation.

3) The power coupling components in the transient stages can be eliminated effectively based on the proposed DFPC method for VSI in the unbalanced system. Simulations and experiment are established to verify the effectiveness of the proposed method. Noted that since the power coupling components in steady state are effectively eliminated by conventional GVM-DPC, this paper focuses on the decoupling strategy under transient stages.

4) Stability of the VSI system is studied by impedance model analysis considering the power decoupling effect.

The rest of this paper is organized as follows. In Section II, the power coupling characteristics of GVM-DPC under unbalanced system are analyzed. In Section III, the traditional GVM-DPC is introduced, and then the power decoupling strategy is proposed. In Section IV, simulations are conducted to validate the effectiveness of the proposed method. A hardware-in-loop (HIL) test performed on RTDS is presented in Section V. Finally, the conclusions are drawn in Section VI.

II. Power Coupling Characteristics of GVM-DPC Connected to an Unbalanced System

Fig. 1 shows the conventional two-level GVM-DPC-based VSI connected to an unbalanced grid voltage system where an asymmetric fault occurs [33]. A stiff DC power source is utilized in this paper, which ignores the dynamic influences from DC side. An inductor in series of resistor constitute the filter of VSI.

In Fig. 1, $\boldsymbol{i}_{\mathrm{L},abc}$ and $\boldsymbol{v}_{\mathrm{pcc},abc}$ are the 3-phase currents and PCC voltages measured for the calculation of instantaneous real and reactive powers in positive and negative sequence (P^{+}_{f}, P^{-}_{f}, Q^{+}_{f}, Q^{-}_{f}), where P^{+}_{f}, Q^{+}_{f} are control inputs of traditional GVM-DPC to regulate output powers according to power references, and P^{-}_{f}, Q^{-}_{f} are the control inputs of PC block to balance the 3-phase currents. Delay signal cancellation method in [39] is used to extract positive and negative sequence components. Please note that there is a strong assumption in conventional GVM-DPC, i.e., the PCC voltages in positive sequence after the band pass filter (BPF) (denoted as $\boldsymbol{v}^{+}_{\mathrm{pccf},\alpha\beta}$) are ideal voltages without considering the angle difference from PCC to V_{g} as shown in Fig. 1 and (1), which will cause serious real and reactive power coupling issues of VSI in the transient stages. In (1), PCC voltages after BPF are represented in α-β reference frame, where V_{pccf} is the magnitude of fundamental voltage, and ω_{f} is the rated angular frequency of the fundamental voltage at PCC.

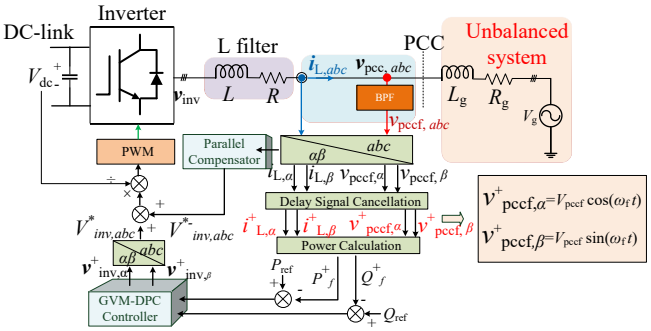

Fig. 1. GVM-DPC diagram for the VSI connected to an unbalanced system.

$$\begin{cases} v^{+}_{\mathrm{pccf},\alpha} = V_{\mathrm{pccf}}\cos(\omega_{\mathrm{f}}t) \\ v^{+}_{\mathrm{pccf},\beta} = V_{\mathrm{pccf}}\sin(\omega_{\mathrm{f}}t) \end{cases} \tag{1}$$

To illustrate the power coupling mechanism under the unbalanced grid voltage system, different sequence components of PCC voltage and current are shown in Fig. 2.

In the unbalanced system, GVM-DPC usually excites the negative and 3rd order positive sequence currents, i.e., $\boldsymbol{i}^{-}_{\mathrm{L}}$, $\boldsymbol{i}^{3+}_{\mathrm{L}}$ shown in Fig. 2(a), which will be eliminated by the PC control block in our control system shown in Fig. 1 to balance the output currents of VSI [33], as shown in Fig. 2. As a result, the PCC voltage ($\boldsymbol{v}_{\mathrm{pccf}}$) contains the positive and negative sequence components ($\boldsymbol{v}^{+}_{\mathrm{pccf}}$, $\boldsymbol{v}^{-}_{\mathrm{pccf}}$) and the output current of VSI ($\boldsymbol{i}_{\mathrm{L}}$) only comprises positive sequence quantity ($\boldsymbol{i}^{+}_{\mathrm{L}}$), as shown in Fig. 2(b). Then, different sequence real and reactive powers can be

derived in (2) as follows, where $\boldsymbol{v}^+_{pccf,\alpha}$, $\boldsymbol{v}^+_{pccf,\beta}$, $i^+_{L,\alpha}$, $i^+_{L,\beta}$ are the positive sequence voltages and currents at PCC and $\boldsymbol{v}^-_{pccf,\alpha}$, $\boldsymbol{v}^-_{pccf,\beta}$ are the negative sequence components.

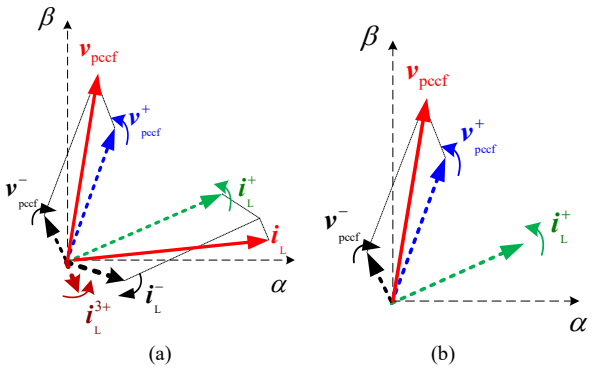

Fig. 2. The phasor diagrams of the relationship between positive and negative sequence PCC voltage and current. (a) is the original vector before the balance of current, and (b) is the vector after the current is balanced.

$$P_{11}=\frac{3}{2}(v^+_{pccf,\alpha}i^+_{L,\alpha}+v^+_{pccf,\beta}i^+_{L,\beta}),P_{12}=\frac{3}{2}(v^-_{pccf,\alpha}i^+_{L,\alpha}+v^-_{pccf,\beta}i^+_{L,\beta})$$
$$Q_{11}=\frac{3}{2}(v^+_{pccf,\beta}i^+_{L,\alpha}-v^+_{pccf,\alpha}i^+_{L,\beta}),Q_{12}=\frac{3}{2}(v^-_{pccf,\beta}i^+_{L,\alpha}-v^-_{pccf,\alpha}i^+_{L,\beta}) \quad (2)$$

It can be observed that the output powers only contain DC components (P_{11}, Q_{11}) and twice-order harmonic components (P_{21}, Q_{21}). Since the magnitude of negative sequence voltage at PCC ($\boldsymbol{v}^-_{pccf}$) is usually smaller than that of positive sequence value ($\boldsymbol{v}^+_{pccf}$) for most asymmetric faults [33], i.e., P_{21}, Q_{21} are far less than P_{11}, Q_{11}, thus this paper only considers the effect of power coupling between P_{11} and Q_{11} shown in Fig. 3 below, whereas the coupling between P_{21} and Q_{21} is not taken into account.

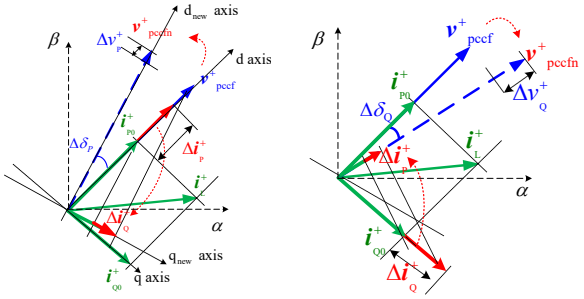

Fig. 3. The phasor diagrams of the power coupling mechanism for positive sequence components including (a) reactive power coupled with real power, and (b) real power coupled with reactive power.

In Fig. 3, the positive sequence PCC voltage ($\boldsymbol{v}^+_{pccf}$) and current ($\boldsymbol{i}^+_L$) are selected to illustrate the coupling terms. The original current in positive sequence before changing $\boldsymbol{i}^+_L$ and its active and reactive components, i.e. $\boldsymbol{i}^+_{P0}$ and $\boldsymbol{i}^+_{Q0}$ are represented by green arrows. The deviation components of $\boldsymbol{i}^+_{P0}$ and $\boldsymbol{i}^+_{Q0}$ denoted as $\Delta\boldsymbol{i}^+_P$, $\Delta\boldsymbol{i}^+_Q$ are represented in red solid arrows, in accordance with power references (P_{ref}, Q_{ref} in Fig. 1) change. In Fig. 3(a), when P_{ref} increases, $\boldsymbol{i}^+_{P0}$ will accordingly increase by $\Delta\boldsymbol{i}^+_P$, as marked by red solid arrow. Then, the positive sequence voltage of PCC will change from $\boldsymbol{v}^+_{pccf}$ to $\boldsymbol{v}^+_{pccfn}$ with a variation of angle difference between PCC voltage and grid voltage ($\Delta\delta_P$) and magnitude deviation Δv^+_P, due to the voltage propagation characteristics along grid side impedance, i.e., $(R_g+j\omega L_g)\cdot\Delta\boldsymbol{i}^+_L$.

As a result, the projection of $\Delta\boldsymbol{i}^+_P$ on the q_{new} axis is not null (denoted as $\Delta\boldsymbol{i}^+_Q$ in Fig. 3(a)), which will increase the reactive power. Thus, coupling reactive power component is produced after considering effect of the $\Delta\delta_P$.

Similarly, in Fig. 3(b), the reactive current $\boldsymbol{i}^+_{Q0}$ will increase by $\Delta\boldsymbol{i}^+_Q$ when the Q_{ref} increases, as marked by red solid arrow. Then, the PCC voltage in positive sequence will changed from $\boldsymbol{v}^+_{pccf}$ to $\boldsymbol{v}^+_{pccfn}$, with an angle variation $\Delta\delta_Q$ and magnitude deviation Δv_Q, as labeled in Fig. 3(b).

As a result, the projection of $\Delta\boldsymbol{i}^+_Q$ on the vector of $\boldsymbol{v}^+_{pccfn}$ is not null (denoted as $\Delta\boldsymbol{i}_P$ in Fig. 3(b)), which is the coupling real power component after considering the effect of voltage angle variation $\Delta\delta_Q$. Please note that $\Delta\delta_P$, $\Delta\delta_Q$ can be analytically quantified and used for the calculation of power coupling magnitudes, which can be utilized as the power compensation for power decoupling of GVM-DPC. This mechanism is explained in detail in Section III-B below.

In conclusion, the neglection of voltage angle variation of PCC in conventional GVM-DPC will certainly lead to power coupling issues. In the following section, the detailed GVM-DPC model is introduced and the power-coupling components are verified according to derivations. Then a power decoupling strategy is proposed to improve the transient performance of GVM-DPC method.

III. The Power Decoupling Strategy for GVM-DPC

A. Limited Capability of Power Decoupling of GVM-DPC

In Fig. 1, one can obtain the state space equation of positive sequence output powers P^+_f, Q^+_f (denoted as P_{11} and Q_{11} in Eq. (2)):

$$\begin{cases}\dfrac{dP^+_f}{dt}=\dfrac{3}{2}(i^+_{L,\alpha}\dfrac{dv^+_{pccf,\alpha}}{dt}+v^+_{pccf,\alpha}\dfrac{di^+_{L,\alpha}}{dt}+i^+_{L,\beta}\dfrac{dv^+_{pccf,\beta}}{dt}+v^+_{pccf,\beta}\dfrac{di^+_{L,\beta}}{dt})\\ \dfrac{dQ^+_f}{dt}=\dfrac{3}{2}(i^+_{L,\alpha}\dfrac{dv^+_{pccf,\beta}}{dt}+v^+_{pccf,\beta}\dfrac{di^+_{L,\alpha}}{dt}-i^+_{L,\beta}\dfrac{dv^+_{pccf,\alpha}}{dt}-v^+_{pccf,\alpha}\dfrac{di^+_{L,\beta}}{dt})\end{cases} \quad (3)$$

where $v^+_{pccf,\alpha}$, $v^+_{pccf,\beta}$ are assumed to be ideal voltages without considering voltage angle variation ($\Delta\delta$) in conventional GVM-DPC, shown in (1). This assumption lacks rationality when VSI connects to weak grids with higher grid side impedance, as discussed in Section II. Thus, the grid voltages can be modified as follows:

$$\begin{cases}v^+_{pccf,\alpha}=V_{pccf}\cos(\omega_f t+\varphi(t))\\ v^+_{pccf,\beta}=V_{pccf}\sin(\omega_f t+\varphi(t))\end{cases} \quad (4)$$

where the angle difference $\varphi(t)$ can be represented as,

$$\varphi(t)=\arctan\frac{P^+_f X_g-Q^+_f R_g}{P^+_f R_g+Q^+_f X_g+(V^+_g)^2} \quad (5)$$

One can differentiate (4) w. r. t. the time t and substitute it into (3):

$$\begin{cases}\dfrac{dP^+_f}{dt}=-\dfrac{R}{L}P^+_f-(\omega_f+\varphi'(t))Q^+_f+\dfrac{3}{2L}u_P\\ \dfrac{dQ^+_f}{dt}=(\omega_f+\varphi'(t))P^+_f-\dfrac{R}{L}Q^+_f+\dfrac{3}{2L}u_Q\end{cases} \quad (6)$$

where u_P and u_Q are defined variables used for feedback linearization method [33]. It can be founded that the coefficient $\omega_f+\varphi'(t)$ in (6) is a time-varying value corresponding to output

powers of VSI (P^+_f, Q^+_f), thus it cannot be decoupled by conventional feedback linearization method in GVM-DPC, i.e. set u_P and u_Q as follows:

$$\begin{cases} u_{\mathrm{P}} = \dfrac{2L\omega_f}{3} Q^+_f + K_{\mathrm{P},\mathrm{p}} e_{\mathrm{P}} + K_{\mathrm{P},\mathrm{i}} \displaystyle\int_0^t e_{\mathrm{P}}(\tau)d\tau \\ u_{\mathrm{Q}} = -\dfrac{2L\omega_f}{3} P^+_f + K_{\mathrm{Q},\mathrm{p}} e_{\mathrm{Q}} + K_{\mathrm{Q},\mathrm{i}} \displaystyle\int_0^t e_{\mathrm{Q}}(\tau)d\tau \end{cases} \tag{7}$$

where e_{P} and e_{Q} are the errors between the reference (P_{ref}, Q_{ref}) and $K_{P,p}$, $K_{P,i}$, $K_{Q,p}$, and $K_{Q,i}$ are the coefficients of PI controllers for real and reactive powers. In the conventional GVM-DPC, the modulated voltages for PWM ($v_{\mathrm{inv},\alpha}$, $v_{\mathrm{inv},\beta}$ shown in Fig. 4) can be obtained by substituting (7) into (8):

$$\begin{cases} v^+_{\mathrm{inv},\alpha} = \dfrac{v^+_{\mathrm{pccf},\alpha} u_P + v^+_{\mathrm{pccf},\beta} u_Q + V^2_{\mathrm{pccf}} v^+_{\mathrm{pccf},\alpha}}{V^2_{\mathrm{pccf}}} \\ v^+_{\mathrm{inv},\beta} = \dfrac{v^+_{\mathrm{pccf},\beta} u_P - v^+_{\mathrm{pccf},\alpha} u_Q + V^2_{\mathrm{pccf}} v^+_{\mathrm{pccf},\beta}}{V^2_{\mathrm{pccf}}} \end{cases} \tag{8}$$

where V_{pccf} is the amplitude of PCC voltage. Please note that substituting (7) into (6) yields:

$$\begin{cases} \dfrac{dP^+_f}{dt} = -\dfrac{R}{L} P^+_f - \varphi'(t) Q^+_f + \dfrac{3}{2L}\left(K_{P,p} e_P + K_{P,i} \displaystyle\int_0^t e_P(\tau)d\tau\right) \\ \dfrac{dQ^+_f}{dt} = \varphi'(t) P^+_f - \dfrac{R}{L} Q^+_f + \dfrac{3}{2L}\left(K_{Q,p} e_Q + K_{Q,i} \displaystyle\int_0^t e_Q(\tau)d\tau\right) \end{cases} \tag{9}$$

Eq. (9) shows that the positive sequence real and reactive powers are not fully decoupled after using feedback linearization. Thus, it is essential to propose a power decoupling method for GVM-DPC-based VSI under unbalanced voltage system, which will be introduced in Section III-*B* as follows. Please note that in the steady state, the phase angle difference of PCC voltage and grid side voltage is nearly a constant value, so its deferential signal $\varphi'(t)$ equals 0. In this case, the real and reactive powers are effectively decoupled in conventional GVM-DPC as shown in (9). Thus, this paper only considers the dynamic process of power coupling issues.

B. *Proposed Power Decoupling Strategy for VSI Connected to the Unbalanced System*

To decouple the coupling components of positive sequence real and reactive powers, two DFPCs are added into the power references in GVM-DPC, i.e., P_{com} and Q_{com}, shown in Fig. 4. The P_{com} and Q_{com} are coupling magnitudes of positive sequence real and reactive powers in accordance with Δi^+_{P} and Δi^+_{Q} in Fig. 3, which is derived as follows.

According to Fig. 3, the output real and reactive powers w.r.t. the active and reactive current deviations ($\Delta \boldsymbol{i}^+_{\mathrm{P}}$ and $\Delta \boldsymbol{i}^+_{\mathrm{Q}}$) are:

$$\begin{cases} P^+_{fn} = \left|\boldsymbol{v}^+_{\mathrm{pccfn}}\right| \cdot \left[\left|\boldsymbol{i}^+_{\mathrm{Q0}} + \Delta \boldsymbol{i}^+_{\mathrm{Q}}\right| \sin\Delta\delta_{\mathrm{Q}} + \left|\boldsymbol{i}^+_{\mathrm{P0}}\right| \cos\Delta\delta_{\mathrm{Q}}\right] \\ Q^+_{fn} = \left|\boldsymbol{v}^+_{\mathrm{pccfn}}\right| \cdot \left[\left|\boldsymbol{i}^+_{\mathrm{P0}} + \Delta \boldsymbol{i}^+_{\mathrm{P}}\right| \sin\Delta\delta_{\mathrm{P}} + \left|\boldsymbol{i}^+_{\mathrm{Q0}}\right| \cos\Delta\delta_{\mathrm{P}}\right] \end{cases} \tag{10}$$

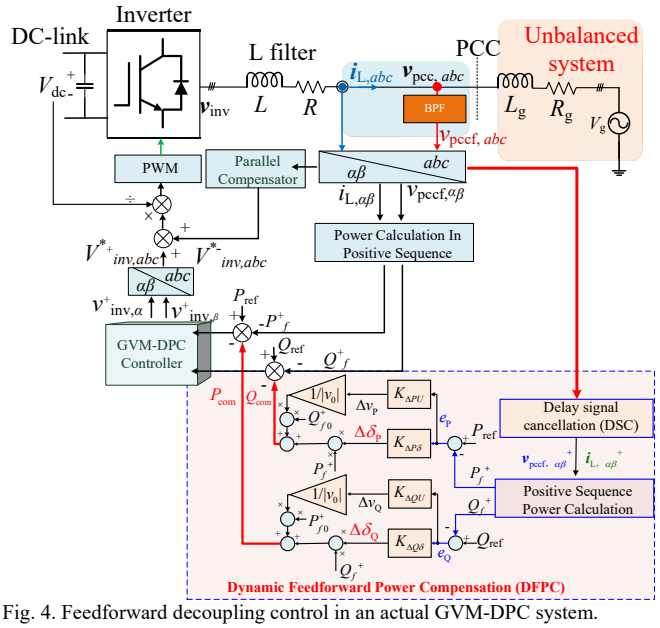

Fig. 4. Feedforward decoupling control in an actual GVM-DPC system.

where P^+_{fn} , Q^+_{fn} are the real and reactive powers of VSI in accordance with currents change by $\Delta \boldsymbol{i}^+_{\mathrm{P}}$ and $\Delta \boldsymbol{i}^+_{\mathrm{Q}}$. $\boldsymbol{v}^+_{\mathrm{pccfn}}$ is the positive sequence voltage at PCC after the changes of $\Delta \boldsymbol{i}^+_{\mathrm{P}}$ or $\Delta \boldsymbol{i}^+_{\mathrm{Q}}$, and the $\boldsymbol{i}^+_{\mathrm{P0}}$ and $\boldsymbol{i}^+_{\mathrm{Q0}}$ represent the corresponding positive sequence currents at equilibrium point. Eq. (10) can be derived based on the analysis of Fig. 3 as follows.

When real power reference (P_{ref} in Fig. 1) increases, active current $\boldsymbol{i}^+_{\mathrm{P0}}$ of i^+_{L} would increase by $\Delta \boldsymbol{i}^+_{\mathrm{P}}$ based on the GVM-DPC, as marked by red solid arrow in Fig. 3(a). Then the positive sequence voltage $\boldsymbol{v}^+_{\mathrm{pccf}}$ will change to $\boldsymbol{v}^+_{\mathrm{pccfn}}$ with angle variation $\Delta\delta_{\mathrm{P}}$ by considering the angle difference on grid side impedance. In this case, the new reactive power Q^+_{fn} can be derived by multiplication of voltage magnitude $|\,\boldsymbol{v}^+_{\mathrm{pccfn}}\,|$ and reactive current: $|\,\boldsymbol{i}^+_{\mathrm{P0}}+\Delta \boldsymbol{i}^+_{\mathrm{P}}\,|\sin\Delta\delta_{\mathrm{P}} + |\,\boldsymbol{i}^+_{\mathrm{Q0}}|\cos\Delta\delta_{\mathrm{P}}$.

Similarly, when reactive power reference (Q_{ref} in Fig. 1) increases, reactive current of i^+_{L} would accordingly increase by $\Delta \boldsymbol{i}^+_{\mathrm{Q}}$, as marked by red solid arrow in Fig. 3(b). Thus, $\boldsymbol{v}^+_{\mathrm{pccf}}$ will increase to $\boldsymbol{v}^+_{\mathrm{pccfn}}$ with angle variation $\Delta\delta_{\mathrm{Q}}$. Then, the new real power P^+_{fn} can be calculated by multiplication of voltage magnitude $|\,\boldsymbol{v}^+_{\mathrm{pccfn}}\,|$ and active current, i.e., $|\,\boldsymbol{i}^+_{\mathrm{Q0}}+\Delta \boldsymbol{i}^+_{\mathrm{Q}}\,|\sin\Delta\delta_{\mathrm{Q}} + |\,\boldsymbol{i}^+_{\mathrm{P0}}|\cos\Delta\delta_{\mathrm{Q}}$.

In (10), the voltage angle variation of angle difference between PCC voltage and grid voltage, i.e. $\Delta\delta_{\mathrm{P}}$ and $\Delta\delta_{\mathrm{Q}}$, are derived as follows:

$$\begin{cases} \Delta\delta_{\mathrm{P}} = K_{\Delta P\delta} \times \Delta P \\ \Delta\delta_{\mathrm{Q}} = K_{\Delta Q\delta} \times \Delta Q \end{cases} \tag{11}$$

where $\Delta P = P_{\mathrm{ref}} - P^+_f$, $\Delta Q = Q_{\mathrm{ref}} - Q^+_f$, and both of them are denoted by e_{P} and e_{Q}, setting as control inputs of the DFPC blocks, as shown in Fig. 4.

The coefficients ($K_{\Delta P\delta}$, $K_{\Delta Q\delta}$) in (11) can be calculated by the inverse of the Jacobian matrix in (12), as shown in (13).

$$\begin{bmatrix} \Delta P \\ \Delta Q \end{bmatrix} = \begin{bmatrix} \dfrac{\partial P}{\partial \delta} & \dfrac{\partial P}{\partial U} \\ \dfrac{\partial Q}{\partial \delta} & \dfrac{\partial Q}{\partial U} \end{bmatrix} \begin{bmatrix} \Delta\delta \\ \Delta U \end{bmatrix} \tag{12}$$

$$\begin{bmatrix} K_{\Delta P\delta} & K_{\Delta Q\delta} \\ K_{\Delta PU} & K_{\Delta QU} \end{bmatrix} = \begin{bmatrix} \dfrac{\partial P}{\partial \delta} & \dfrac{\partial P}{\partial U} \\ \dfrac{\partial Q}{\partial \delta} & \dfrac{\partial Q}{\partial U} \end{bmatrix}^{-1} \tag{13}$$

Therefore, for the positive sequence network, the elements in the Jacobian matrix in (12) can be analytically expressed at the equilibrium point [34]:

$$\begin{cases} \dfrac{\partial P}{\partial \delta} = \dfrac{1}{R_g{}^2 + X_g{}^2}\left(-\left|\boldsymbol{v}^+_{\text{pccf}}\right| V_g R_g \sin\delta_0 + \left|\boldsymbol{v}^+_{\text{pccf}}\right| V_g X_g \cos\delta_0\right) \\ \dfrac{\partial P}{\partial U} = \dfrac{1}{R_g{}^2 + X_g{}^2}\left(V_g R_g \cos\delta_0 + V_g X_g \sin\delta_0\right) \\ \dfrac{\partial Q}{\partial \delta} = \dfrac{1}{R_g{}^2 + X_g{}^2}\left(-\left|\boldsymbol{v}^+_{\text{pccf}}\right| V_g R_g \sin\delta_0 - \left|\boldsymbol{v}^+_{\text{pccf}}\right| V_g X_g \cos\delta_0\right) \\ \dfrac{\partial Q}{\partial U} = \dfrac{1}{R_g{}^2 + X_g{}^2}\left(V_g X_g \cos\delta_0 - V_g R_g \sin\delta_0\right) \end{cases} \tag{14}$$

where $\boldsymbol{v}^+_{\text{pccf}}$ can be measured by using conventional delay signal cancellation (DSC) [39], which can extract positive and negative sequence signals by introducing a 1/4 period time delay shown in Fig. 5. $x^{(\alpha\beta)}(t)$ is a time-series signal in α-β reference frame. $x_{\text{P}}{}^{(\alpha\beta)}(t)$ and $x_{\text{N}}{}^{(\alpha\beta)}(t)$ are the corresponding positive and negative sequence signals.

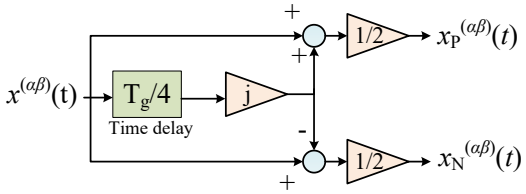

Fig. 5. Delay signal cancellation

In (14), δ_0 represents the steady-state angle difference between positive sequence components of PCC voltage ($\boldsymbol{v}^+_{\text{pccf}}$) and grid side voltage ($V^+_{\text{g}}\angle 0$), which can be pre-calculated by PMU measuring. Also, the grid side impedance (R_g, X_g) can be measured by online impedance detection techniques [42]-[44].

Finally, the DFPC for real power channel, i.e., $P_{\text{com}} = P^+_{fn} - P^+_{f0}$ can be obtained as (15), where P^+_{f0} is the positive sequence real power at equilibrium point. $|\,\boldsymbol{v}^+_{\text{pccfn}}\,|$ is the amplitude of positive sequence voltage, and Δv denotes its amplitude deviation derived as (16), where $K_{\Delta PU}$ and $K_{\Delta QU}$ can be obtained by (13).

$$\begin{aligned} P_{\text{com}} &= \left|\boldsymbol{v}^+_{\text{pccfn}}\right| \cdot \left[\left|\boldsymbol{i}^+_{\text{Q0}} + \Delta\boldsymbol{i}^+_{\text{Q}}\right| \sin\Delta\delta_{\text{Q}} + \left|\boldsymbol{i}^+_{\text{P0}}\right| \cos\Delta\delta_{\text{Q}}\right] - P^+_{f0} \\ &= Q^+_f \sin\Delta\delta_{\text{Q}} + \left(1 + \frac{\Delta v^+_{Q}}{\left|\boldsymbol{v}^+_{\text{pccfn}}\right|}\right) P^+_{f0} \cos\Delta\delta_{\text{Q}} - P^+_{f0} \end{aligned} \tag{15}$$

$$\begin{cases} \Delta v_{\text{P}} = K_{\Delta PU} \times \Delta P \\ \Delta v_{\text{Q}} = K_{\Delta QU} \times \Delta Q \end{cases} \tag{16}$$

For the simplification of real power compensation, $\sin\Delta\delta_{\text{P}}$ and $\cos\Delta\delta_{\text{P}}$ in (15) are linearized as $\Delta\delta_{\text{P}}$ and 1, respectively. Then, (15) is simplified to (17) based on (11) and (16), where Q^+_f is the positive sequence reactive power of VSI.

$$P_{\text{com}} \approx K_{\Delta Q\delta} Q^+_f e^+_{\text{Q}} + \frac{K_{\Delta QU} e^+_{\text{Q}}}{|\,\boldsymbol{v}^+_{\text{pccf}}\,|} P^+_{f0} \tag{17}$$

Similarly, the reactive power compensation block can be simplified to (18), where P^+_f is the measured positive sequence real power of VSI.

$$Q_{\text{com}} \approx K_{\Delta P\delta} P^+_f e^+_{\text{P}} + \frac{K_{\Delta PU} e^+_{\text{P}}}{|\,\boldsymbol{v}^+_{\text{pccf}}\,|} Q^+_{f0} \tag{18}$$

Please note that the proposed method will not affect the steady-state performance and ripple cancelation of GVM-DPC, since it only extract positive sequence PCC voltage and current to generate coupling real and reactive powers as two compensation components for GVM-DPC, and the power errors (denoted as P_{ref}-P^+_f, Q_{ref}-Q^+_f in Fig. 4) are zero in steady-state, so the outputs of the proposed DFPC block are nearly zero, which will not affect the steady-state performance.

C. Discussion of Proposed Power Decoupling Strategy

Most of the power decoupling researches focus on power coupling mechanism in the high resistance/inductance ratio (R/X) connecting line systems [24]-[29], indicating that when the resistance equals inductance, the power coupling of VSI will be severer. On the contrary, when the connecting line from VSI to power grid is inductive, the powers will be decoupled. Thus, the virtual inductance methods are proposed to reshape the connecting line to be inductive by adding a virtual inductance into the VSG control loop. However, the decoupling performance can be deteriorated since the method only considers the effect of impedance angle, ignoring the influences from PCC voltage angle variation and its magnitude perturbation when the output powers of VSI change, which is illustrated by phasor diagram in Fig. 3 of our paper. Please note that the power coupling in positive sequence is severer even the connecting line is inductive, and its proof is shown in Appendix, where some conclusions can be drawn from (44):

i) If the VSI is connected to a strong grid where grid side inductance is small enough (i.e., $X_{\text{g}} \approx 0$), the output powers of VSI can be fully decoupled since the real power only depends on active current and reactive power only depends on reactive current.

ii) On the contrary, if the VSI is connected to a weak grid where grid side inductance X_{g} increases, the coupling coefficients between real power and reactive current, reactive power and active current will increase accordingly, indicating the severer occurrence of power coupling.

D. Stability Analysis of GVM-DPC-based VSI in Unbalanced System based on Impedance Model

The stability of the control system under unbalanced grid voltage condition is analyzed in this section based on the impedance model. Firstly, the impedance model of VSI system is established in part (1) where the closing loop relationship between PCC voltage and current is described, then the Nyquist stability criteria is introduced in part (2) based on the impedance model. Please note that the VSI terminal voltage is separately controlled in positive and negative sequence under unbalanced grid voltage system, where positive sequence terminal voltage is controlled as (8) shown and negative sequence terminal voltage is controlled in traditional PC block to eliminate negative sequence output currents as shown in [19]. The VSI stability can be guaranteed when both positive and negative sequence impedance models satisfy Nyquist stability criteria. In this paper, only positive sequence impedance is introduced

since this paper only considers the power decoupling effect in positive sequence system, which is proved that it will not affect negative sequence impedance in this section. The negative sequence impedance can be derived in a similar way.

(1) *Impedance Model of VSI Considering Power Decoupling Effect*

Firstly, the dynamics of VSI terminal voltage $\boldsymbol{v}^{+}_{\text{inv}}$ in terms of $\boldsymbol{v}^{+}_{\text{pcc}}$ and $\boldsymbol{i}^{+}_{\text{L,abc}}$ under stationary reference frame should be deduced. By substituting (7) into (8), the terminal voltage can be derived as:

$$\begin{cases} \boldsymbol{v}^{+}_{\text{inv},\alpha} = L(K_{\text{p}}(A_\alpha + B_\alpha) + K_{\text{i}}D_\alpha + C_\alpha) + \boldsymbol{v}^{+}_{\text{pcef},\alpha} \\ \boldsymbol{v}^{+}_{\text{inv},\beta} = L(K_{\text{p}}(A_\beta + B_\beta) + K_{\text{i}}D_\beta + C_\beta) + \boldsymbol{v}^{+}_{\text{pcef},\beta} \end{cases} \tag{19}$$

where A_α, A_β, B_α, B_β, C_α, C_β, D_α and D_β can be represented as (20), (21). K_{p} and K_{i} are parameters of PI controller, which are denoted with $K_{P,p}$, $K_{P,i}$, $K_{Q,p}$, and $K_{Q,i}$ in (7).

$$\begin{aligned} A_\alpha &= -\frac{2(P^{+}_{f}v^{+}_{\text{pcef},\alpha} + Q^{+}_{f}v^{+}_{\text{pcef},\beta})}{3\left|\boldsymbol{v}^{+}_{\text{pcef}}\right|^2}, A_\beta = -\frac{2(P^{+}_{f}v^{+}_{\text{pcef},\beta} - Q^{+}_{f}v^{+}_{\text{pcef},\alpha})}{3\left|\boldsymbol{v}^{+}_{\text{pcef}}\right|^2} \\ B_\alpha &= \frac{2(P_{\text{ref}}v^{+}_{\text{pcef},\alpha} + Q_{\text{ref}}v^{+}_{\text{pcef},\beta})}{3\left|\boldsymbol{v}^{+}_{\text{pcef}}\right|^2}, \quad B_\beta = \frac{2(P_{\text{ref}}v^{+}_{\text{pcef},\beta} - Q_{\text{ref}}v^{+}_{\text{pcef},\alpha})}{3\left|\boldsymbol{v}^{+}_{\text{pcef}}\right|^2} \\ C_\alpha &= -\frac{2\omega_s(P^{+}_{f}v^{+}_{\text{pcef},\beta} - Q^{+}_{f}v^{+}_{\text{pcef},\alpha})}{3\left|\boldsymbol{v}^{+}_{\text{pcef}}\right|^2}, C_\beta = \frac{2\omega_s(Q^{+}_{f}v^{+}_{\text{pcef},\beta} + P^{+}_{f}v^{+}_{\text{pcef},\alpha})}{3\left|\boldsymbol{v}^{+}_{\text{pcef}}\right|^2} \end{aligned} \tag{20}$$

$$\begin{aligned} D_\alpha &= \frac{2v^{+}_{\text{pcef},\alpha}}{3\left|\boldsymbol{v}^{+}_{\text{pcef}}\right|^2}\int(P_{\text{ref}} - P^{+}_{f}) + \frac{2v^{+}_{\text{pcef},\beta}}{3\left|\boldsymbol{v}_{\text{pcef}}\right|^2}\int(Q_{\text{ref}} - Q^{+}_{f}) \\ D_\beta &= \frac{2v^{+}_{\text{pcef},\beta}}{3\left|\boldsymbol{v}_{\text{pcef}}\right|^2}\int(P_{\text{ref}} - P^{+}_{f}) - \frac{2v^{+}_{\text{pcef},\alpha}}{3\left|\boldsymbol{v}_{\text{pcef}}\right|^2}\int(Q_{\text{ref}} - Q^{+}_{f}) \end{aligned} \tag{21}$$

Substituting instantaneous powers P_{11}, Q_{11} in (2) into (19) to simplify A_α, A_β, C_α and C_β as follows,

$$A_\alpha = i^{+}_{\text{L},\alpha}, A_\beta = i^{+}_{\text{L},\beta}, C_\alpha = \omega_f i^{+}_{\text{L},\beta}, C_\beta = -\omega_f i^{+}_{\text{L},\alpha} \tag{22}$$

For the linearization of B_α and B_β, the transfer function of Band-Pass Filter (BPF) in Fig. 1 is defined as:

$$F_{\text{f}} = \frac{2\zeta\omega_{\text{fn}}s}{s^2 + 2\zeta_{\text{f}}\omega_{\text{fn}}s + \omega_{\text{fn}}^2} \tag{23}$$

where ω_{fn} and ζ_{f} are the natural frequency and damping ratio of BPF. The coefficients B_α, B_β can be linearized as (24), assuming that the $|\boldsymbol{v}^{+}_{\text{pccfb}}|^2$ is a constant value after the BPF [30].

$$\begin{aligned} B_\alpha &\approx \frac{2P_{\text{ref}}}{3\left|\boldsymbol{v}^{+}_{\text{pccfb}}\right|^2}v^{+}_{\text{pcef},\alpha} + \frac{2Q_{\text{ref}}}{3\left|\boldsymbol{v}^{+}_{\text{pccfb}}\right|^2}v^{+}_{\text{pcef},\beta} \\ B_\beta &\approx \frac{2P_{\text{ref}}}{3\left|\boldsymbol{v}^{+}_{\text{pccfb}}\right|^2}v^{+}_{\text{pcef},\beta} - \frac{2Q_{\text{ref}}}{3\left|\boldsymbol{v}^{+}_{\text{pccfb}}\right|^2}v^{+}_{\text{pcef},\alpha} \end{aligned} \tag{24}$$

For the linearization of D_α and D_β, P^{+}_{f} and Q^{+}_{f} are presented as (25) where $\odot$ and $\otimes$ denote the dot product and cross product of two complex vectors. P_{dc} and Q_{dc} are DC components where subscript b in $\boldsymbol{i}^{+}_{\text{L,b}}$, $\boldsymbol{v}^{+}_{\text{pcc,b}}$ denotes fundamental frequency component. P_{ac} and Q_{ac} are harmonics with oscillation frequency ω_{f}-ω_{h}, where ω_{f} is fundamental frequency and ω_{h} is the harmonic frequency. $\boldsymbol{v}^{+}_{\text{pcc}}$ and $\boldsymbol{i}^{+}_{\text{L}}$ can be written as (26), (27), where subscripts h denotes the harmonic order.

$$\begin{aligned} P_f &\approx \underbrace{\left(-\frac{3}{2}\boldsymbol{i}^{+}_{\text{L,b}} \odot \boldsymbol{v}^{+}_{\text{pcc,b}}\right)}_{P_{\text{dc}}} + \underbrace{\left(-\frac{3}{2}\boldsymbol{i}^{+}_{\text{L,h}} \odot \boldsymbol{v}^{+}_{\text{pcc,b}}\right)}_{P_{\text{ac}}} \\ Q_f &\approx \underbrace{\left(-\frac{3}{2}\boldsymbol{i}^{+}_{\text{L,b}} \otimes \boldsymbol{v}^{+}_{\text{pcc,b}}\right)}_{Q_{\text{dc}}} + \underbrace{\left(-\frac{3}{2}\boldsymbol{i}^{+}_{\text{L,h}} \otimes \boldsymbol{v}^{+}_{\text{pcc,b}}\right)}_{Q_{\text{ac}}} \end{aligned} \tag{25}$$

$$\begin{aligned} \boldsymbol{v}^{+}_{\text{pcc}} &= \boldsymbol{v}^{+}_{\text{pcc,b}} + \boldsymbol{v}^{+}_{\text{pcef,h}} \\ &= v^{+}_{\text{pcc},\alpha\text{b}} + \sum_{\text{h}=1}^{N} F_{\text{f}}(j\omega_{\text{h}})\boldsymbol{v}^{+}_{\text{pcc},\alpha\text{h}} + j\left(v^{+}_{\text{pcc},\beta\text{b}} + \sum_{\text{h}=1}^{N} F_{\text{f}}(j\omega_{\text{h}})\boldsymbol{v}^{+}_{\text{pcc},\beta\text{h}}\right) \end{aligned} \tag{26}$$

$$\boldsymbol{i}^{+}_{\text{L}} = \boldsymbol{i}^{+}_{\text{L,b}} + \boldsymbol{i}^{+}_{\text{L,h}} = i^{+}_{\text{L},\alpha\text{b}} + \sum_{\text{h}=1}^{N} i^{+}_{\text{L},\alpha\text{h}} + j\left(i^{+}_{\text{L},\beta\text{b}} + \sum_{\text{h}=1}^{N} i^{+}_{\text{L},\beta\text{h}}\right) \tag{27}$$

From (21), (25), it can be assumed that the integrals of P_{ref}-P_{dc} and Q_{ref}-Q_{dc} are approximately zero in steady states, i.e., $\int P_{\text{dc}} \approx \int P_{\text{ref}}$, $\int Q_{\text{dc}} \approx \int Q_{\text{ref}}$, which will not affect the harmonic stability of the control system. However, this approximation lacks rationality when real or reactive power changes, since the power coupling components still exist and shown in (17), (18) above. When P_{ref} changes, one can obtain D_α and D_β by substituting coupling reactive power component in (18) into (21):

$$\begin{aligned} D_\alpha &= \frac{2v^{+}_{\text{pcef},\alpha}}{3\left|\boldsymbol{v}^{+}_{\text{pcef}}\right|^2}\int(P_{\text{ref}} - P_{\text{dc}}) + \frac{2v^{+}_{\text{pcef},\alpha}}{3\left|\boldsymbol{v}^{+}_{\text{pcef}}\right|^2}\int(-P_{\text{ac}}) + \\ &\frac{2v_{\text{pcef},\beta}}{3\left|\boldsymbol{v}^{+}_{\text{pcef}}\right|^2}\underbrace{\int((K_{\Delta P\delta}P^{+}_{f} + \frac{K_{\Delta PU}}{\left|\boldsymbol{v}^{+}_{\text{pcef}}\right|}Q^{+}_{f0}) \times (P_{\text{ref}} - P_{\text{dc}}))}_{Q\text{coupling}} + \frac{2v^{+}_{\text{pcef},\beta}}{3\left|\boldsymbol{v}^{+}_{\text{pcef}}\right|^2}\int(-Q_{\text{ac}}) \end{aligned} \tag{28}$$

$$\begin{aligned} D_\beta &= \frac{2v_{\text{pcef},\beta}}{3\left|\boldsymbol{v}_{\text{pcef}}\right|^2}\int(P_{\text{ref}} - P_{\text{dc}}) + \frac{2v_{\text{pcef},\alpha}}{3\left|\boldsymbol{v}_{\text{pcef}}\right|^2}\int(-P_{\text{ac}}) + \\ &\frac{2v_{\text{pcef},\beta}}{3\left|\boldsymbol{v}_{\text{pcef}}\right|^2}\underbrace{\int((K_{\Delta P\delta}P_{f} + \frac{K_{\Delta PU}}{\left|\boldsymbol{v}_{\text{pcef}}\right|}Q_{f0}) \times (P_{\text{ref}} - P_{\text{dc}}))}_{Q\text{coupling}} + \frac{2v_{\text{pcef},\beta}}{3\left|\boldsymbol{v}_{\text{pcef}}\right|^2}\int(-Q_{\text{ac}}) \end{aligned} \tag{29}$$

Noted that $\int(P_{\text{ref}} - P_{\text{dc}})$ and $\int((K_{\Delta P\delta}P^{+}_{f} + K_{\Delta PU}Q^{+}_{f0}/|\boldsymbol{v}^{+}_{\text{pccf}}|) \times (P_{\text{ref}}\text{-}P_{\text{dc}}))$ in (28), (29) are nonzero when P_{ref} begins to change, which will definitely affect the transient stability in harmonic domain. However, they are complicated time-varying variables corresponding to the operation state of VSI, so it is hard to linearize D_α and D_β in (28), (29) at a certain operation point. Thus, in order to study the transient stability of traditional GVM-DPC, Lyapunov method can be proposed to study the stability under the effect of power coupling, which can be a future work of this paper. Nevertheless, the stability of the proposed DFPC-based GVM-DPC can be analyzed by impedance model, since the complicated integral term is effectively reduced to nearly zero by adding DFPC power decoupling components, i.e., $\int(P_{\text{ref}}\text{-}P_{\text{dc}}) \approx 0$, $\int(Q_{\text{ref}}\text{-}Q_{\text{dc}}) \approx 0$. Then, in transient stage, D_α and D_β can be linearized as shown in (30) after utilizing the power decoupling method.

$$\begin{aligned} D_\alpha &\approx -\frac{2}{3}\frac{v^{+}_{\text{pcef},\alpha}Q_{\text{ac}} - v^{+}_{\text{pcef},\beta}P_{\text{ac}}}{\left|\boldsymbol{v}^{+}_{\text{pcef}}\right|^2(\omega_{\text{f}} - \omega_{\text{h}})} \approx -\sum_{\text{h}=1}^{N}\frac{i^{+}_{\text{L},\ \beta\text{h}}}{\omega_{\text{f}} - \omega_{\text{h}}} \\ D_\beta &\approx -\frac{2}{3}\frac{v^{+}_{\text{pcef},\alpha}P_{\text{ac}} - v^{+}_{\text{pcef},\beta}Q_{\text{ac}}}{\left|\boldsymbol{v}^{+}_{\text{pcef}}\right|^2(\omega_{\text{f}} - \omega_{\text{h}})} \approx \sum_{\text{h}=1}^{N}\frac{i^{+}_{\text{L},\ \alpha\text{h}}}{\omega_{\text{f}} - \omega_{\text{h}}} \end{aligned} \tag{30}$$

Finally, the transfer matrix of $\boldsymbol{i}^{+}_{\mathrm{L}}$ and $\boldsymbol{v}^{+}_{\mathrm{pcc}}$ to $\boldsymbol{v}^{+}_{\mathrm{inv}}$ can be derived by substituting (22), (24), (30) into (19), shown as (37). Considering the harmonic components relation of $\boldsymbol{v}^{+}_{\mathrm{inv}}$ and $\boldsymbol{v}^{+}_{\mathrm{pcc}}$ shown in (31), (37) can be reorganized as (32), where $\boldsymbol{Z}_{\mathrm{VSI}}$ represents the impedance model of the proposed DFPC-based VSI system. Similarly, when Q_{ref} changes, power coupling components in (17) in D_α and D_β can be decoupled and the impedance is the same as shown in Eq. (32).

$$\begin{bmatrix} v^{+}_{\mathrm{pcc},\alpha\mathrm{h}} \\ v^{+}_{\mathrm{pcc},\beta\mathrm{h}} \end{bmatrix} = \underbrace{\begin{bmatrix} R+sL & 0 \\ 0 & R+sL \end{bmatrix}}_{\boldsymbol{Z}_{\mathrm{si}}} \begin{bmatrix} i^{+}_{\mathrm{L},\alpha\mathrm{h}} \\ i^{+}_{\mathrm{L},\beta\mathrm{h}} \end{bmatrix} + \begin{bmatrix} v^{+}_{\mathrm{inv},\alpha\mathrm{h}} \\ v^{+}_{\mathrm{inv},\beta\mathrm{h}} \end{bmatrix} \tag{31}$$

$$\begin{bmatrix} v^{+}_{\mathrm{pcc},\alpha\mathrm{h}} \\ v^{+}_{\mathrm{pcc},\beta\mathrm{h}} \end{bmatrix} = \underbrace{\left(\boldsymbol{I}-\boldsymbol{T}_{\mathrm{cv}}\right)^{-1}\left(\boldsymbol{Z}_{\mathrm{si}}+\boldsymbol{Z}_{\mathrm{ci}}\right)}_{\boldsymbol{Z}_{\mathrm{VSI}}} \begin{bmatrix} i^{+}_{\mathrm{L},\alpha\mathrm{h}} \\ i^{+}_{\mathrm{L},\beta\mathrm{h}} \end{bmatrix} \tag{32}$$

(2) *Stability Criteria*

The impedance model in (32) is transformed into a sequence-domain diagonal matrix by using the method proposed in [30], then the stability can be estimated by SISO Nyquist stability criteria.

Equation (32) can be generally expressed as follows:

$$\begin{bmatrix} v_{\mathrm{pcc},\alpha\mathrm{h}} \\ v_{\mathrm{pcc},\beta\mathrm{h}} \end{bmatrix} = \boldsymbol{Z}_{\mathrm{VSI}} \begin{bmatrix} i_{\mathrm{L},\alpha\mathrm{h}} \\ i_{\mathrm{L},\beta\mathrm{h}} \end{bmatrix}, \boldsymbol{Z}_{\mathrm{VSI}} = \begin{bmatrix} Z_{\alpha\alpha} & Z_{\alpha\beta} \\ Z_{\beta\alpha} & Z_{\beta\beta} \end{bmatrix} \tag{33}$$

The equivalent sequence domain impedance can be derived as,

$$\begin{aligned} Z_{\mathrm{VSI,p}}(s) &= \frac{Z_{\alpha\alpha}(s)+Z_{\beta\beta}(s)}{2} + j\frac{Z_{\beta\alpha}(s)-Z_{\alpha\beta}(s)}{2} \\ Z_{\mathrm{VSI,n}}(s) &= \frac{Z_{\alpha\alpha}(s)-Z_{\beta\beta}(s)}{2} + j\frac{Z_{\beta\alpha}(s)+Z_{\alpha\beta}(s)}{2} \end{aligned} \tag{34}$$

where subscripts p and n denote positive and negative sequence components. The negative sequence impedance is zero due to the symmetrical characteristic of the impedance matrix, i.e., $Z_{\alpha\alpha}(s)=Z_{\beta\beta}(s)$, $Z_{\beta\alpha}(s)=-Z_{\alpha\beta}(s)$, only $Z_{\mathrm{VSI,p}}$ is selected for stability analysis. Please note that the zero $Z_{\mathrm{VSI,n}}$ indicates that the positive sequence voltage will not induce negative sequence current, and negative sequence impedance will not be affected by the proposed DFPC values in positive sequence.

The weak grid impedance can be derived as follows:

$$Z_{\mathrm{grid}}(s) = L_{\mathrm{g}}s + R_{\mathrm{g}} \tag{35}$$

Then, the closed-loop transfer function H_{s} can be derived as (36):

$$H_s = \frac{1}{1+G_{\alpha\beta}(s)} \tag{36}$$

where $G_{\alpha\beta}(s)=Z_{\mathrm{grid}}(s)/Z_{\mathrm{VSI,p}}(s)$ is the feedback characteristic equation, which can be treated as the open-loop transfer function of H_s. According to linear-control theory, the stability of the close-loop transfer function H_{s} can be guaranteed if the open-loop transfer function $G_{\alpha\beta}(s)$ satisfies the Nyquist stability criterion.

IV. Case Study

In this section, case study is carried out in MATLAB/Simulink, Simscape Power Systems to verify the proposed power decoupling method for GVM-DPC under unbalanced voltage system shown in Fig. 4. The parameters of controller and grid system are shown in Table I.

TABLE I
System Parameters in the Simulation Systems

Symbol	Parameter	Value	Unit
V_{g}	Nominal grid voltage	133	V
V_{dc}	DC-link voltage	250	V
f	Nominal grid frequency	50	Hz
R	Filter resistor	0.12	Ω
L	Filter inductance	10	mH
R_{g}	Grid side resistor	0.12	Ω
L_{g}	Grid side inductance	1	mH
f_{sw}	Switching frequency	10	kHz
K_{p}	Proportional control parameter of PI controller	10000	
K_{i}	Integral control parameter of PI controller	10000	

First, in Subsection A, the coupling situation of GVM-DPC is tested under the unbalanced grid voltage condition with phase-A dropping to 0.9 p. u.. In this case, coupling components of positive sequence real and reactive powers are presented, which are the control inputs of the proposed DFPC power decoupling method. Also, the power decoupling performance of the DFPC is presented. In subsection B, C, different voltage drop magnitudes and power references are tested to verify the effectiveness of decoupling performance, and in Subsection D, the robustness of DFPC-based VSI is validated by setting grid side impedance parameter mismatches and distorted grid voltage conditions.

A. Phenomenon of Power Coupling under Unbalanced Grid Voltage Condition

The performance of power coupling of VSI under unbalanced grid voltage condition (phase-A dropping to 0.9 p. u.) using the traditional GVM-DPC is presented in Fig. 6, where

$$\begin{bmatrix} v^{+}_{\mathrm{inv},\alpha\mathrm{h}} \\ v^{+}_{\mathrm{inv},\beta\mathrm{h}} \end{bmatrix} = \underbrace{\begin{bmatrix} LK_{\mathrm{p}} & -\dfrac{K_{\mathrm{i}}L}{\omega_{\mathrm{f}}-s/j}+\omega_{\mathrm{f}}L \\ \dfrac{K_{\mathrm{i}}L}{\omega_{\mathrm{f}}-s/j}-\omega_{\mathrm{f}}L & LK_{\mathrm{p}} \end{bmatrix}}_{\boldsymbol{Z}_{\mathrm{ci}}} \begin{bmatrix} i^{+}_{\mathrm{L},\alpha\mathrm{h}} \\ i^{+}_{\mathrm{L},\beta\mathrm{h}} \end{bmatrix} + \underbrace{\begin{bmatrix} \dfrac{2P_{\mathrm{ref}}LK_{\mathrm{p}}F_{\mathrm{f}}(s)}{3\left|v_{\mathrm{pccfb}}\right|^2}+F_{\mathrm{f}}(s) & \dfrac{2LK_{\mathrm{p}}Q_{\mathrm{ref}}F_{\mathrm{f}}(s)}{3\left|v_{\mathrm{pccfb}}\right|^2} \\ -\dfrac{2LK_{\mathrm{p}}Q_{\mathrm{ref}}F_{\mathrm{f}}(s)}{3\left|v_{\mathrm{pccfb}}\right|^2} & \dfrac{2P_{\mathrm{ref}}LK_{\mathrm{p}}F_{\mathrm{f}}(s)}{3\left|v_{\mathrm{pccfb}}\right|^2}+F_{\mathrm{f}}(s) \end{bmatrix}}_{\boldsymbol{T}_{\mathrm{cv}}} \begin{bmatrix} v^{+}_{\mathrm{pcc},\alpha\mathrm{h}} \\ v^{+}_{\mathrm{pcc},\beta\mathrm{h}} \end{bmatrix} \tag{37}$$

in Fig. 6(a) the coupling magnitude of reactive power Q increases to 200Var when P reference is changed from 500W to 2000W at 0.1s, and in Fig. 6(b) the real power coupling magnitudes reaches 500W when Q reference is changed from 0Var to 2000Var at 0.25s. Please note that the second order power ripples (P_{12}, Q_{12} in (2)) cannot be eliminated when output currents of VSI are controlled to be balanced as shown in real and reactive power figures (P, Q) in Fig. 6, thus, the real and reactive powers of VSI cannot be directly utilized as the control inputs of DFPC-based control block, which will

introduce more harmonic components into the output powers of VSI. Alternatively, positive sequence real and reactive powers (P_{seq}, Q_{seq}) can be calculated via DSC as the control inputs of DFPC, which avoids the influences of power ripples on decoupling operation as shown in Fig. 6. In Fig. 6(c), (d), the coupling components (ΔP and ΔQ) of real and reactive powers are reduced from 500W and 200Var to zero respectively when DFPC is adopted, with 100% effective reduction. It is noted that when the coupling powers are reduced to the power ranges: P_{ref} ± 100W or Q_{ref} ± 100Var, the coupling magnitudes (ΔP and ΔQ in figures) are assumed to be zero.

Also, the steady-state performance of output powers after utilizing the proposed DFPC method is discussed as follows. For the reactive power, as shown in Fig. 6(a), (c), the magnitude of power ripple after using DFPC is 100Var when real power increases from 500W to 2000W at 0.1s, which is almost the same with that of conventional GVM-DPC. For the steady-state operation of real power as shown in P of Fig. 6(b), (d), the power ripple magnitude is 100W after using DFPC when reactive power increases from 0Var to 2000Var at 0.25s, which is nearly the same with that of GVM-DPC. Moreover, it can be seen that small amounts of harmonics are included in the output powers in steady state after using the proposed method, but it is within an acceptable range which could also be eliminated by output filter design of VSI.

B. Phenomenon of Power Coupling under Different Voltage Drop Magnitudes

To test the decoupling performance of the proposed method under grid conditions with different voltage drop magnitudes, phase-A voltage magnitude is set to be 0.9 p. u., 0.8 p. u., 0.7 p. u., and 0.6 p. u., respectively, shown in Fig. 7 below. From Fig. 7(a), (b), it can be observed that when the real power increases from 500W to 2000W at 0.1s, the reactive power coupling magnitudes ΔQ are nearly the same, both of which reach 150Var under 0.9 p. u. and 0.8 p. u. phase-A voltage conditions. After utilizing the proposed DFPC method, the reactive power coupling magnitudes ΔQ are reduced to zero, with 100% reduction performance, as shown in Q_{decoup} in Fig. 7(a), (b).

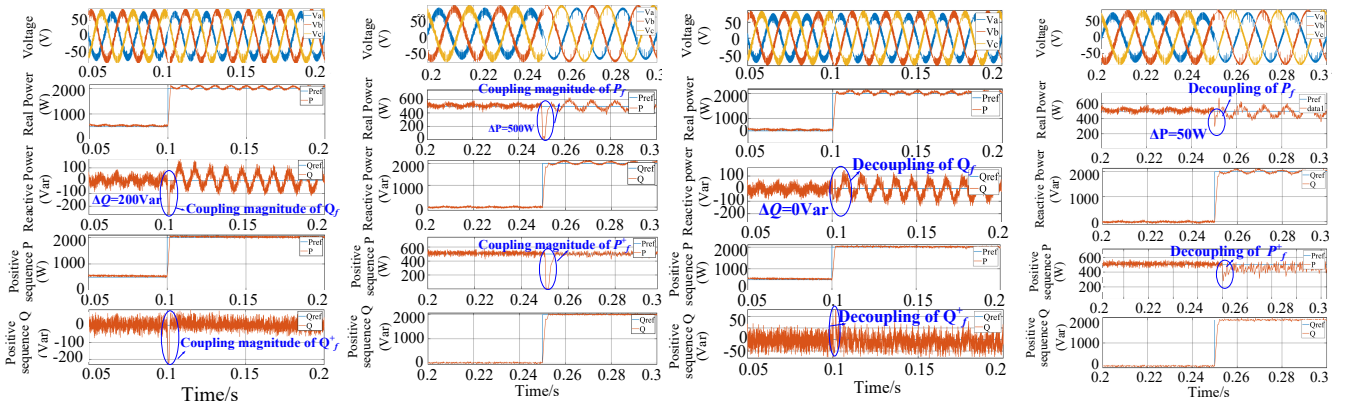

Fig. 6. Dynamic comparison of VSI using traditional GVM-DPC and the proposed DFPC method under the unbalanced voltage system with phase-A drop to 0.9 p. u. (a) reactive power coupling when real power changes, (b) real power coupling when reactive power changes, (c) reactive power decoupling result by the proposed DFPC, and (d) real power decoupling result by the DFPC.

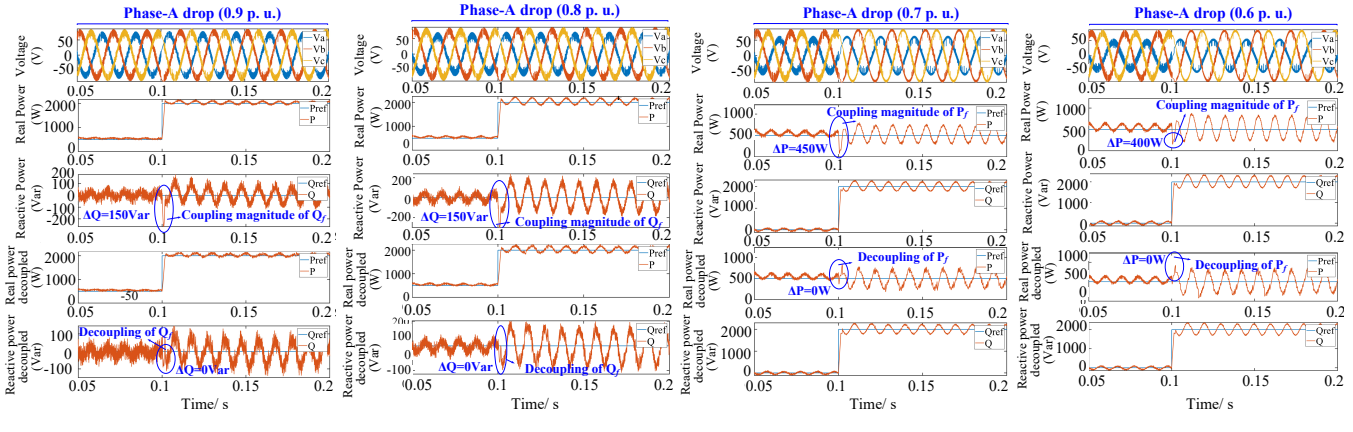

Fig. 7. Performance of VSI power coupling by traditional GVM-DPC and the decoupling results by the proposed control method under different voltage drop magnitudes. (a) and (b) are reactive power coupling results of traditional GVM-DPC and decoupling results by DFPC under grid voltage conditions with 0.9 p. u. and 0.8 p. u. phase-A voltages. (c) and (d) are real power coupling result of GVM-DPC and decoupling results by DFPC under 0.7 p. u. and 0.6 p. u. phase-A voltages.

From Fig. 7(c), (d), when reactive powers increase from 0Var to 2000Var at 0.1s, the real power coupling magnitudes ΔP are 450 W and 400W respectively under 0.7 p. u. and 0.6 p. u. phase-A voltage conditions, and they are reduced to zero with 100% reduction after adopting the proposed method. Please note that larger power ripples exist in steady state when the voltage drops from 0.9 p. u. to 0.6 p. u. as seen from real and reactive power figures in Fig. 7(a)-(d), due to the occurrence of the larger negative sequence voltages in output powers P_{12}, Q_{12} in (2). Moreover, from Fig. 7 it can be seen that there is no impact on steady-state performance and power ripple cancelation performance after using the proposed power decoupling method, as analyzed in Fig. 6 above. Nevertheless, this paper only considers the power coupling issues of positive sequence real and reactive powers in transient stages, the steady state power ripples are not the focus.

C. Performance of Power Decoupling under Different Power References of GVM-DPC

In this section, power decoupling performance with different power references in GVM-DPC under grid condition with two-phase-to-ground fault (Phase A&B voltage drop to 0.9 p. u.) is tested and shown in Fig. 8, where in Fig. 8(a) the real power P increases from 500W to 1400W, 1800W, 2200W at 0.1s, respectively. It can be founded that, the coupling magnitudes of reactive power increases in accordance with the increases of real power references, reaching the maximum value of ΔQ=210Var, as shown in the zoom in figure of Q (denoted as Q_{zoom} in Fig. 8(a)). In Fig. 8(b), the coupling magnitudes of real power increases as well when reactive powers Q increase from 0Var to 2200Var at 0.1s, reaching the maximum value of ΔP=480W, as shown in P_{zoom} in Fig. 8(b). Fig. 8(c) and (d) show the decoupling results of real and reactive powers after using the proposed method. It can be seen that the reactive power coupling magnitude ΔQ is reduced from 210Var to 0Var with ideally 100% reduction capability, and the real power coupling magnitude ΔP is reduced from 480W to 30W, with 93% reduction performance.

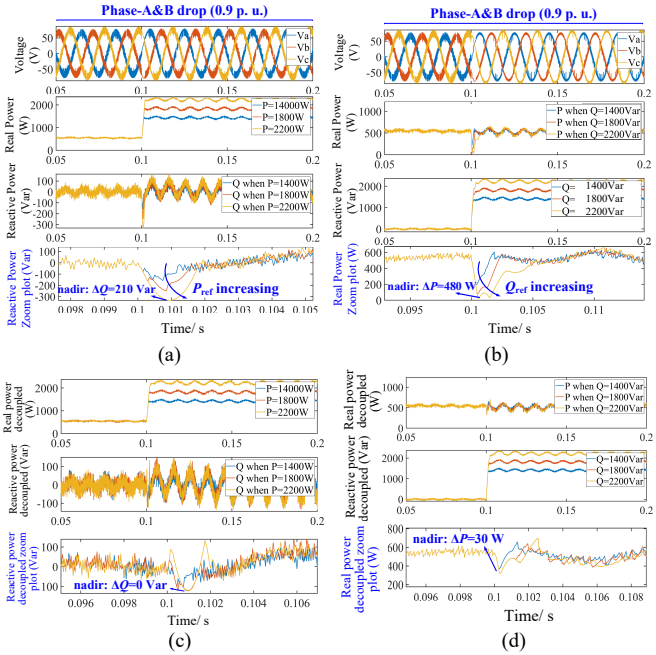

Fig. 8. Performance of power decoupling under different power references in GVM-DPC when two-phases-to-ground fault occurs. (a) and (b) are power coupling results in GVM-DPC when P changes from 500W to 1.4kW, 1.8kW, 2.2kW and Q changes from 0 Var to 1.4kVar, 1.8kVar, 2.2kVar. (c) and (d) are power decoupling results in accordance with (a) and (b).

D. Robustness of the Proposed DFPC under Parameter Mismatch and Harmonic Distorted Grid Voltage Condition

As described in (14), the grid side impedance R_g, L_g is required for the DFPC-based power decoupling method. Hence, it is necessary to test the robustness of the proposed method under different percentage of errors of parameter mismatches, as shown in Fig. 9(a). It can be seen that the coupling magnitude of reactive power (ΔQ) reaches 150Var when real power increases from 500W to 2000W at 0.1s. After using the proposed DFPC method with accurate parameter detection, ΔQ drops to 0Var with 100% reduction performance. However, when the parameter mismatch error is set to be 20% and 30%,

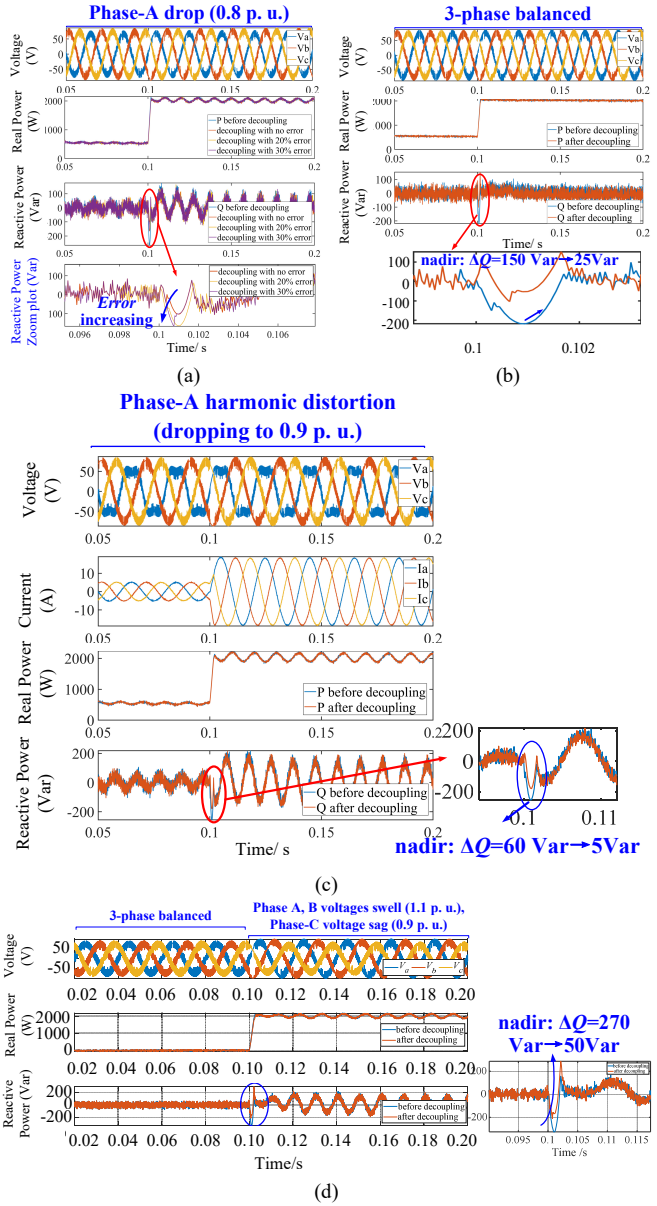

Fig. 9. Robustness of GVM-DPC with DFPC under harmonic distorted grid voltage condition and parameter mismatches. (a) is the coupling and decoupling results under 3-phase voltage balanced condition. (b) is the coupling and

decoupling results with parameter mismatches reaching 30% errors under unbalanced system. (c) is the coupling and decoupling results under unbalanced system when a 3rd harmonic component is emulated for phase-A voltage. (d) is the power decoupling results of the proposed method under voltage swell system when single-phase-to-ground fault occurs.

the coupling magnitudes will be increased from 0Var to 50Var, with 67% reduction performance of decoupling, which is still within acceptable range. Besides, different grid voltage conditions with 3-phase balanced voltages and harmonic distorted voltage are also explored, as shown in Fig. 9(b), (c). From (b), it can be seen that the proposed method is also suitable for the balanced voltage condition, which can effectively reduce the coupling magnitude of reactive power from ΔQ=150Var to ΔQ=25Var when real power increase from 500W to 2000W at 0.1s, with 83% reduction performance. From Fig. 9(c), a 3rd order harmonic component is set for phase-A voltage with maximum magnitude of 0.9 p. u. It can be observed that the coupling magnitude of reactive power can be reduced from ΔQ=60Var to ΔQ=5Var with 91% reduction. Consequently, the robustness of the proposed DFPC method against different voltage conditions and parameter mismatch is verified. Finally, voltage swell condition is also tested in this section, which often occurs as a result of single-phase-to-ground (SPTG) fault in an ungrounded system. From Fig. 9(d), the SPTG fault happens at 0.1s, with phase-A, B voltages swelling to 1.1 p. u., and phase-C voltage dropping to 0.9 p. u.. It can be seen that when real power increases to 2000W at 0.1s, the coupling reactive power magnitude is effectively reduced from 270Var to 50Var, with 81% reduction performance.

Noted that the large power ripple in Fig.7, 8, 9 cannot be further eliminated when output 3-phase currents are controlled to be balanced and sinusoidal in this paper, thus the output powers are mostly 2nd order harmonic components denoted by P_{12}, Q_{12} as shown in (2). It has already been proved that the ripples in real and reactive powers cannot be eliminated simultaneously [12]. Normally, there are 3 control methods to constrain power ripples, e.g., maintaining the sinusoidal currents, keeping constant real power, or removing the ripples of reactive power [12]. This paper selects the first control scheme to obtain the 3-phase balanced-sinusoidal currents, so the power ripples in real and reactive powers cannot be fully eliminated.

E. Comparison with traditional virtual-inductance-based power decoupling method

Conventional virtual impedance method (VIM) for virtual synchronous generator control (VSG) is selected as a comparison to clarify the contribution of the proposed DFPC method for GVM-DPC [24]. The VIM is widely adopted in VSG to reshape the predominately inductive connecting line so as to reduce the coupling magnitudes.

As discussed in Section III-C, the "predominant inductive line" indicator cannot reduce the coupling magnitudes when grid side impedance increases in weak grids, since it only considers the effect of impedance angle without considering voltage angle variation and its amplitude perturbation when injected powers change. To verify this, Fig. 10 shows the power decoupling results of VSG-based VSI using VIM and GVM-DPC-based VSI with the proposed DFPC in the unbalanced system (phase-A voltage amplitude dropping to 0.9 p. u.). The control parameters of GVM-DPC can be seen in Table I, and VSG refers to [24], [45]. The grid side impedance is set to be 12mH, which is large enough to test the drawback of VIM. From Fig.10(a), (b), when real power of VSG-based VSI increases to 1 p. u. at 1s with virtual impedance x_v=0 p. u., the reactive power decreases from 0 to -0.24 p. u. accordingly. When x_v increases from 0 to 0.6 p. u., coupling magnitudes of reactive powers increase as well, indicating that more reactive powers will be absorbed by VSI from power grids which will eventually leads to system destabilization. However, the coupling reactive power can be effectively decoupled by the proposed DFPC method, with magnitude dropping from 0.22 p. u. to 0.03 p. u., as shown in Fig. 10(d).

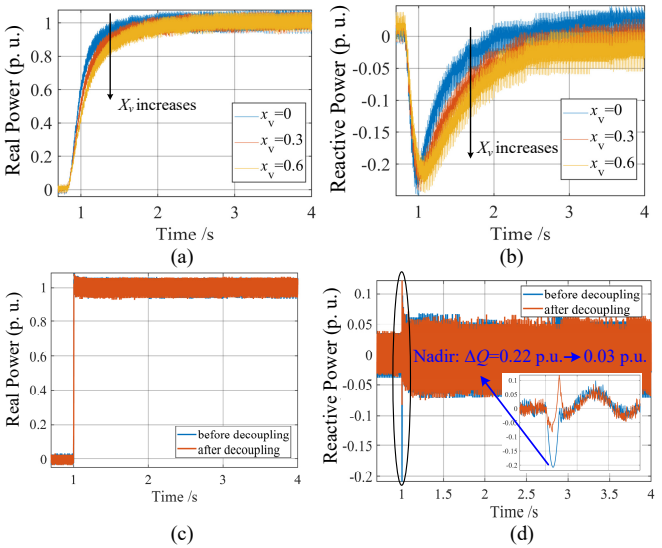

Fig.10. Comparison of power decoupling performance of VSG-based VSI using VIM and GVM-DPC-based VSI using the proposed DFPC method. (a), (b) are real and reactive powers of VSG-based VSI using different virtual impedances. (c), (d) are real and reactive powers of GVM-DPC-based VSI using the proposed method.

F. Stability case study

The stability of the proposed control system is tested in this case, which is studied by the Nyquist stability analysis on $G_{\alpha\beta}(s)$.

For a weak grid system with phase-A voltage dropping to 0.9 p. u., the grid side impedance is set to be 10mH. All the parameters are set according to Table I above. When the VSI is controlled to output real powers from 0W to 1000W, 1300W, 1400W and 1500W respectively, the Nyquist diagram near the critical point (-1, 0) is drawn in Fig. 11 below. It can be seen that, when the P_{ref} increases from 1000W to 1400W, characteristic loci of $G_{\alpha\beta}(s)$ move close to the critical point without encircling it, indicating the systems are stable. However, the locus begins to encircle the critical point when P_{ref}=1500W, indicating that the system begins to destabilize.

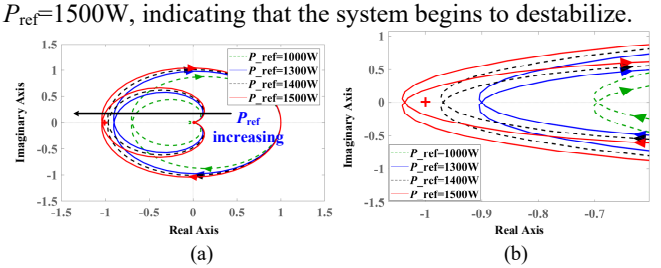

Fig.11. Nyquist diagram of $G_{\alpha\beta}(s)$ under different power references after power decoupling. (a) is the Nyquist diagram and (b) is its zoom in plot near critical point.

A time-domain simulation is carried out to prove the correctness of stability analysis. Fig. 12 shows the stability performance of the GVM-DPC-based VSI system when P_{ref} changes from 0W to 1000, 1300, 1400 and 1500W at 0.1s, respectively, where Fig. 12(a) shows the conventional GVM-DPC performance and Fig. 12(b) shows the simulation results of the proposed DFPC-based VSI system. From Fig. 12(b), it can be seen that when P_{ref} changes from 0W to 1000, 1300, and 1400W at 0.1s, the systems are still stable while it is destabilized when P_{ref} reaches 1500W. Simulation results of DFPC-based VSI show consistency with the impedance analysis.

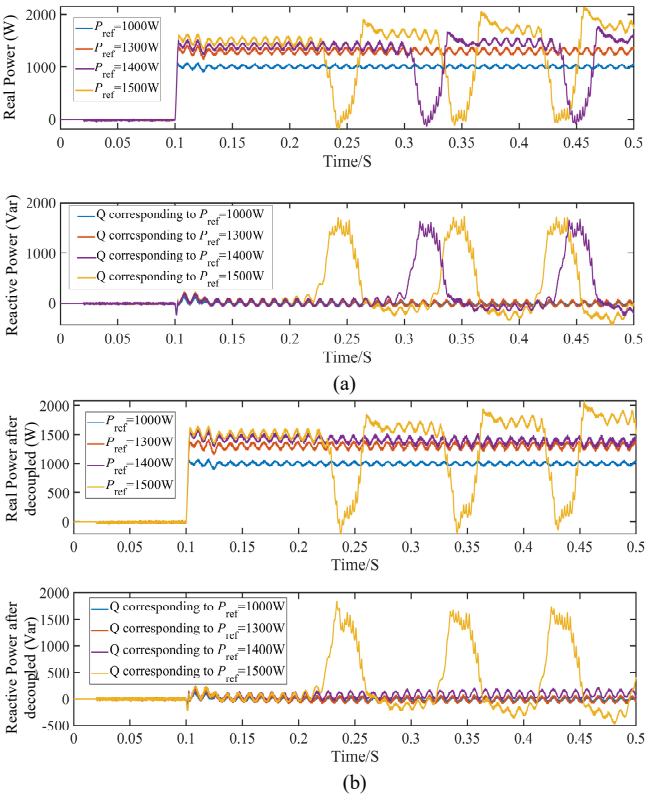

Fig.12. Real and reactive powers when rated real powers are 1000W, 1300W, and 1500W. (a), (b) are powers before power decoupling and (c), (d) are powers after power decoupling.

V. Hardware In Loop Test

The proposed DFPC power decoupling strategy is also validated through an HIL test system shown in Fig. 13. The control parameters and grid side impedance can be changed via communications with a control computer. The grid-connected VSI using GVM-DPC and DFPC scheme is represented by detailed EMT models in the RTDS. The proposed DFPC method is implemented in VSI control system established in RSCAD. The sampling time is 1 μs to capture the switching dynamics of converter. Also, the PC control block is included in the system to control negative sequence real and reactive powers to be zero, so as to obtain 3-phase balanced output currents of VSI. To eliminate the positive sequence quantity, the delay signal cancellation (DSC) method [39] is adopted in PC control block for the sequence separation. The DSC extracts the positive and negative sequence with a time delay of 1/4 of the signal period, which is widely used to improve PLL or VSI control under unbalanced grid conditions [39]-[41].

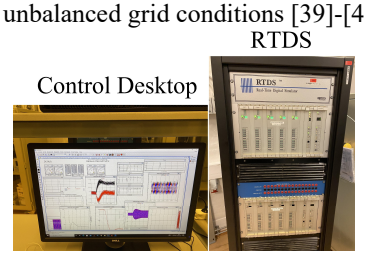

Fig. 13. HIL test setup with RTDS

Two different cases are tested, i.e., balanced grid voltage condition and single-phase-to-ground fault condition. For the balanced system, the proposed DFPC method can effectively eliminate coupling powers in the transient stage, as shown in Fig. 14(a) below. It can be observed that when real power increases from 0W to 2kW at 0.4s, the coupling magnitude of reactive power reaches 1200Var at 0.45s. When the proposed method is utilized, the coupling magnitude of reactive power is reduced from 1200Var to 0Var at 0.45s, with 100% reduction of coupling component. Besides, the dynamic of real power is improved by using the proposed method.

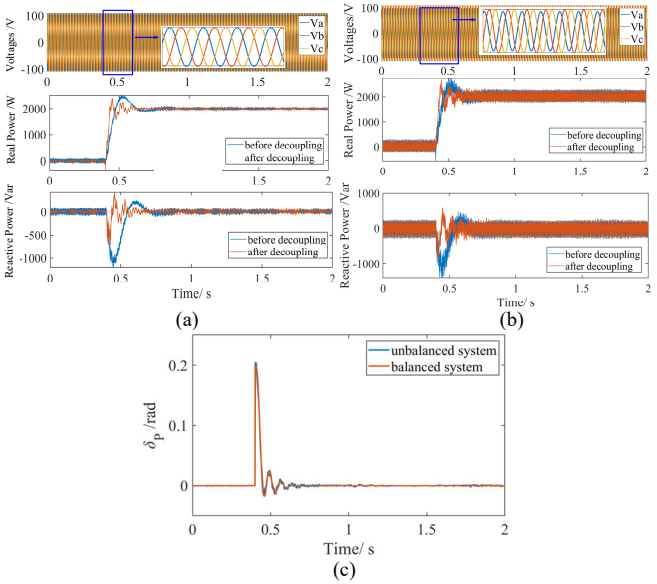

Fig. 14. Power decoupling performance under different grid voltage conditions. (a) is 3-phase voltages balanced system and (b) is the unbalanced system. (c) is the angle variation result (δ_P) when P_{ref} change from 0W to 2000W.

For the unbalanced grid voltage system with phase-A drops to 0.9 p. u., the decoupling performance is verified and shown in Fig. 14(b). From Fig. 14(b), it can be seen that large power ripples are produced due to the unbalanced grid voltage system. When real power increases from 0W to 2kW at 0.4s, the coupling magnitude of reactive power reaches 1300Var at 0.45s. When the proposed DFPC is utilized for GVM-DPC, the coupling magnitude is reduced to nearly zero at 0.45s with 100% reduction performance. Fig, 14(c) shows the trajectories of the angle difference of PCC voltage and grid side voltage in positive sequence denoted by $\Delta\delta_P$ in Fig. 3 above. It can be seen that the $\Delta\delta_P$ increases from 0rad to 0.2 rad when real power rises

from 0W to 2000W at 0.4s, which indicates the occurrence of power coupling in that short period. Then it decreases to zero when real power remains at a steady state, and the power coupling component does not exist in this situation.

VI. Experimental Results

An experimental setup is established to validate the effectiveness of the proposed power decoupling method. A 3-leg 3-phase 1kVA Danfoss inverter with an L filter is connected to a chroma grid simulator via a grid side inductor as Fig. 15 shown. The control strategy is implemented in dSPACE1006 system to generate PWM signals for VSI, where the switching pulses are generated via DS5101 digital waveform output board. The unbalanced grid voltage condition is set in grid simulator with phase-B dropping to 0.9 p. u.. The signals are measured by LEM boards as shown in Fig. 15(a) with sampling frequency of 10kHz. All the parameters are set according to Table II.

TABLE II
System Parameters in the Experimental Setup

Symbol	Parameter	Value	Unit
V_g	Nominal line-to-line grid voltage	133	V
V_{dc}	DC-link voltage	250	V
f	Nominal grid frequency	50	Hz
R	Filter resistor	0	Ω
L	Filter inductance	7.2	mH
R_g	Grid side resistor	0	Ω
L_g	Grid side inductance	1.8mH	mH
f_{sw}	Switching frequency	10	kHz
f_a	Sampling frequency	10	kHz
K_p	Proportional control parameter of PI controller	12000	
K_i	Integral control parameter of PI controller	3000	

As seen in Fig. 16 (a)(b), the output 3-phase currents are balanced under the unbalanced voltage system based on the PC control block in Fig. 1. From Fig. 16(c), it can be observed that coupling reactive power is produced when real power increases from 0W to 550W, with coupling magnitude of 160Var. Then, the coupling reactive power decreases to zero when the VSI system operates in the steady states. After utilizing the proposed power decoupling method, the coupling magnitude of reactive power (ΔQ) reduces to zero with 100% reduction performance, as shown in Fig. 16(d). Moreover, it can be seen that the steady-state performances of real and reactive powers are not distorted by the proposed method, which mainly include twice order harmonic ripple with period 0.01s, as shown in Fig. 16 (c)(d). Also, small amounts of higher order harmonics can be seen in real power in steady states before and after decoupling as shown in Fig. 16 (c)(d), due to the harmonic distortion in voltage condition.

For the discussion of robustness of the proposed method, different parameter mismatches are set in the proposed DFPC control system, and the VSI operates in a harmonic distorted unbalanced voltage condition. From Fig. 17(a), it can be observed that the reactive power compensation magnitude is larger than realistic coupling magnitude when the estimated grid side inductance is larger than real value with +20% error (estimated value: 2.16mH, realistic value: 1.8mH), as a result, ΔQ increases from 0Var in Fig. 16(d) to 25Var in Fig. 17(a), with 70% reduction performance (original ΔQ=83Var). When the estimated inductance is lower than realistic value with -25% error (estimated value: 1.35mH, realistic value: 1.8mH), the ΔQ equals 20Var, with 75% reduction performance. To sum up, the proposed method still could eliminate over 70% coupling magnitude under 25% parameter mismatch.

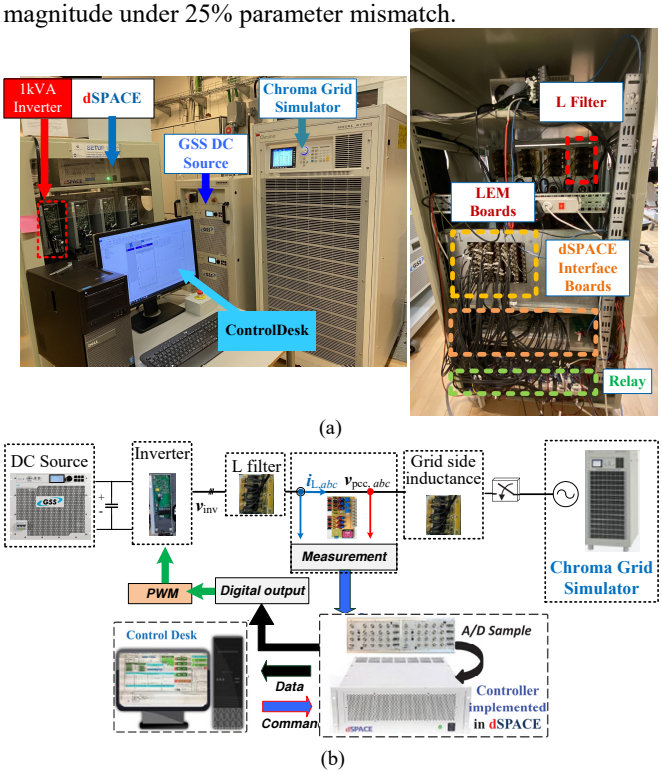

Fig. 15. (a) Experimental setup for power decoupling control verification. (b) Generic system architecture.

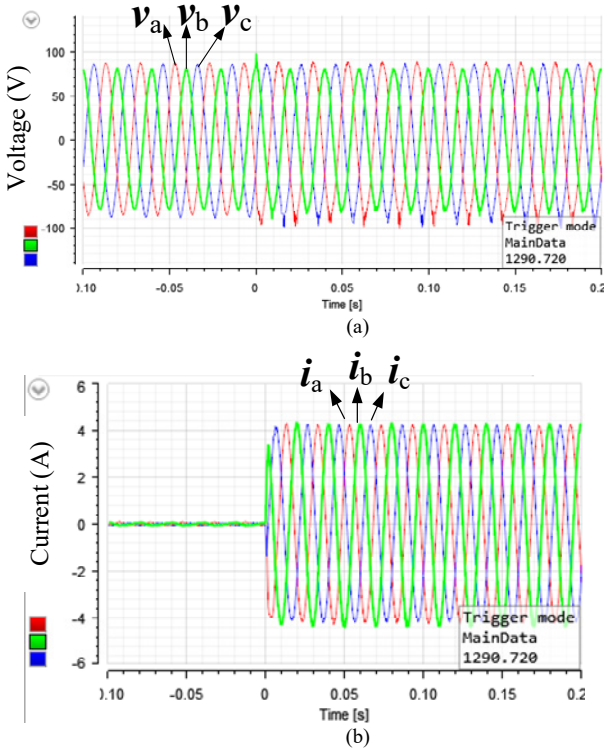

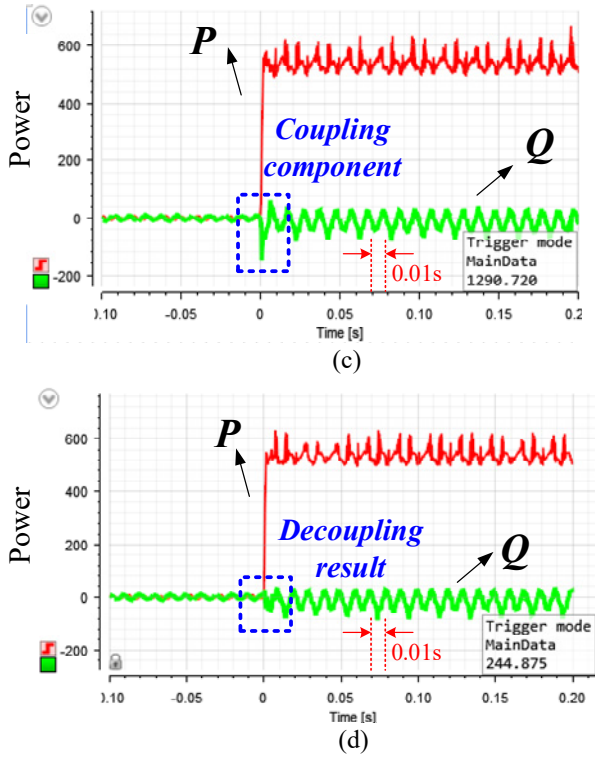

Fig. 16. Test results of the proposed power decoupling method. (a), (b) are 3-phase voltages and currents at PCC detected by LEM board under unbalanced grid voltage condition with phase-B dropping to 0.9 p. u.; (c) and (d) are the coupling component of reactive power and the decoupling performance of the proposed method.

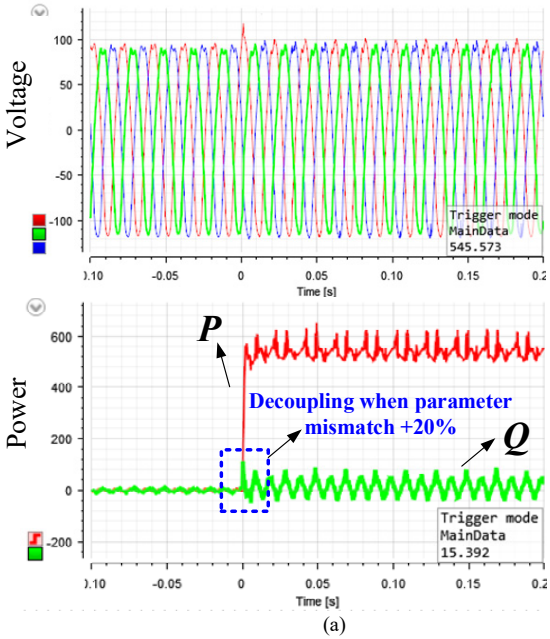

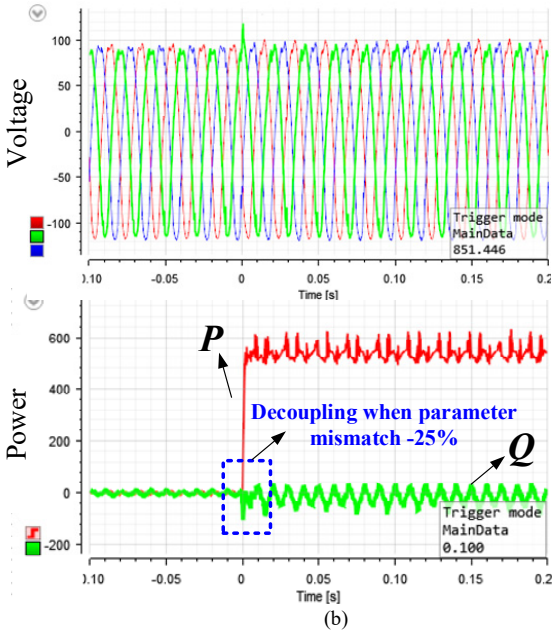

Fig. 17. Robustness test when impedance parameters mismatches varying from +20% to -25% under harmonic distorted system. (a) is power decoupling performance under +20% parameter mismatch. (b) is power decoupling result under -25% parameter mismatch.

VII. Conclusions and Future Work

This paper proposes a power decoupling method for GVM-DPC of the three-phase VSI connected to the weak grids under unbalanced grid voltage system, where the DFPC is implemented into the power control loop in GVM-DPC to compensate the coupling powers. Compared with the traditional GVM-DPC, the proposed method can effectively eliminate the power coupling issues in weak grids with consideration of positive sequence component of PCC voltage variations. Case studies show that the proposed method can reduce over 80% coupling magnitudes of both real and reactive powers for the normal power regulation of VSI under unbalanced voltage condition with different voltage drop from 0.9 p. u. to 0.6 p. u.. Besides, the robustness of the proposed DFPC is verified in terms of harmonic distorted unbalanced grid voltage and parameter mismatches, with performance of over 67% reduction of coupling powers considering 30% error of parameter mismatch and over 90% reduction of coupling powers under harmonic distorted unbalanced grid voltages. Also, experimental work validates the proposed power decoupling method under normal and harmonic distorted system, indicating that the reduction of coupling components performance can be over 70% under 25% parameter mismatch errors. Moreover, impedance analysis of the VSI system is conducted after the powers are decoupled in the transient stage, and case study result using different control parameters verifies the stability analysis. The power decoupling of multiple VSIs based on the GVM-DPC constitutes the future work.

Appendix

To prove the power coupling phenomenon of VSI connected to the unbalanced grid voltage system via inductive connecting line, the R_g is set to zero in Fig. 1. The relationship of positive sequence components of PCC voltage, active and reactive

currents is given as (38)

$$v_{\text{pccf}}^{+}\angle\delta = jX_g(i_{\text{P}}^{+} - ji_{Q}^{+}) + V_g^{+}\angle 0 \tag{38}$$

where the PCC voltage amplitude is given by (39) and it can be linearized according to active and reactive currents as shown in (40).

$$v_{\text{pcc}}^{+} = V_g^{+} + jX_g i_{\text{P}}^{+} + X_g i_{Q}^{+} = \sqrt{(V_g^{+} + X_g i_{Q}^{+})^2 + (X_g i_{\text{P}}^{+})^2} \tag{39}$$

$$\Delta v_{\text{pcc}}^{+} = \left(\frac{X_g^2 i_{\text{P0}}^{+}}{\sqrt{(V_g^{+} + X_g i_{\text{Q0}}^{+})^2 + (X_g i_{\text{P0}}^{+})^2}}\right)\Delta i_{\text{P}}^{+} + \left(\frac{(V_g^{+} + X_g i_{\text{Q0}}^{+})X_g}{\sqrt{(V_g^{+} + X_g i_{\text{Q0}}^{+})^2 + (X_g i_{\text{P0}}^{+})^2}}\right)\Delta i_{\text{Q}}^{+} \tag{40}$$

Meanwhile, the output real power P^{+} can be linearized in accordance with PCC voltage amplitude $\Delta v_{\text{pcc}}^{+}$ and active current i_{p}^{+}:

$$\Delta P^{+} = i_{P0}^{+}\Delta v_{\text{pcc}}^{+} + v_{\text{pcc0}}^{+}\Delta i_{P}^{+} \tag{41}$$

Substituting (40) into (41) yields,

$$\Delta P^{+} = \left(\frac{X_g i_{P0}^{+2}}{\sqrt{V_g^{+2}/X_g^{2} + 2V_g^{+} i_{Q0}^{+}/X_g + i_{Q0}^{+2} + i_{P0}^{+2}}} + v_{\text{pcc0}}^{+}\right)\Delta i_{P}^{+} + \left(\frac{(V_g^{+} + X_g i_{Q0}^{+})i_{P0}^{+}}{\sqrt{V_g^{+2}/X_g^{2} + 2V_g^{+} i_{Q0}^{+}/X_g + i_{Q0}^{+2} + i_{P0}^{+2}}}\right)\Delta i_{Q}^{+} \tag{42}$$

Similarly, the linearization of reactive power can be derived,

$$\Delta Q^{+} = \left(\frac{X_g i_{P0}^{+} i_{Q0}^{+}}{\sqrt{V_g^{+2}/X_g^{2} + 2V_g^{+} i_{Q0}^{+}/X_g + i_{Q0}^{+2} + i_{P0}^{+2}}}\right)\Delta i_{P}^{+} + \left(\frac{(V_g^{+} + X_g i_{Q0}^{+})i_{Q0}^{+}}{\sqrt{V_g^{+2}/X_g^{2} + 2V_g^{+} i_{Q0}^{+}/X_g + i_{Q0}^{+2} + i_{P0}^{+2}}} + v_{\text{pcc0}}^{+}\right)\Delta i_{Q}^{+} \tag{43}$$

Finally, positive sequence power coupling of VSI can be expressed by (44), where c is shown in (45).

$$\begin{bmatrix}\Delta P^{+}\\ \Delta Q^{+}\end{bmatrix} = \begin{bmatrix}\frac{X_g i_{P0}^{+2}}{c} + v_{\text{pcc0}}^{+} & \frac{(V_g^{+} + X_g i_{Q0}^{+})i_{P0}^{+}}{c}\\ \frac{X_g i_{P0}^{+} i_{Q0}^{+}}{c} & \frac{(V_g + X_g i_{Q0}^{+})i_{Q0}^{+}}{c} + v_{\text{pcc0}}^{+}\end{bmatrix}\begin{bmatrix}\Delta i_{P}^{+}\\ \Delta i_{Q}^{+}\end{bmatrix} \tag{44}$$

$$c = \sqrt{V_g^{+2}/X_g^{2} + 2V_g^{+} i_{Q0}^{+}/X_g + i_{Q0}^{+2} + i_{P0}^{+2}} \tag{45}$$

REFERENCES

[1] Q. Liu, T. Caldognetto, S. Buso, "Review and comparison of grid-tied inverter controllers in microgrids," *IEEE Trans. Power Electron*, vol. 35, no. 7, pp. 7624-7639, July 2020.

[2] W. Yao, M. Chen, J. M. Guerrero, and Z.-M. Qian, "Design and analysis of the droop control method for parallel inverters considering the impact of the complex impedance on the power sharing," *IEEE Trans. Ind. Electron.*, vol. 58, no. 2, pp. 576—588, Feb. 2011.

[3] C. Liu and J. Han, "Evaluation of the Sub-Synchronous Control Interaction Based on the Elastic Energy Equivalent System," *IEEE Trans. Power Systems*, 2022, doi: 10.1109/TPWRS.2022.3204070.

[4] L. Shang, X. Dong, C. Liu, Z. Gong, "Fast grid frequency and voltage control of battery energy storage system based on the amplitude-phase-locked-loop," *IEEE Trans. Smart Grid*, vol. 13, no. 2, pp. 941-953. 2022.

[5] Y. P. Siwakoti, F. Z. Peng, F. Blaabjerg, *et al*., "Impedance-source networks for electric power conversion part II: review of control and modulation techniques," *IEEE Trans. Power Electron*, vol. 30, no. 4, pp. 1887-1906, April 2015.

[6] A. K. Bhattacharjee, N. Kutkut, I. Batarseh, "Review of multiport converters for solar and energy storage integration," *IEEE Trans. Power Electron*, vol. 34, no. 2, pp. 1431-1445, Feb. 2019.

[7] L. Shang, X. Dong, C. Liu, *et al.*, "Fast grid frequency and voltage control of battery energy storage system based on the amplitude-phase-locked-loop," *IEEE Trans. Smart Grid*, vol. 13, no. 2, pp. 941-953, March 2022.

[8] M. Malinowski, M. Jasi´nski, and M. P. Kazmierkowski, "Simple direct power control of three-phase PWM rectifier using space-vector modulation (DPC-SVM)," *IEEE Trans. Ind. Electron*., vol. 51, no. 2, pp. 447–454, Apr. 2004.

[9] G. Abad, M. A. Rodriguez, and J. Poza, "Two-level VSC based predictive direct torque control of the doubly fed induction machine with reduced torque and flux ripples at low constant switching frequency," *IEEE Trans. Power Electron*., vol. 23, no. 3, pp. 1050-1061, May 2008.

[10] T. Noguchi, H. Tomiki, S. Kondo, and I. Takahashi, "Direct power control of PWM converter without power-source voltage sensors," *IEEE Trans. Ind. Appl.*, vol. 34, no. 3, pp. 473-479, May/Jun. 1998.

[11] J. Hu, L. Shang, Y. He, and Z. Zhu, "Direct active and reactive power regulation of grid-connected DC/AC converters using sliding mode control approach," *IEEE Trans. Power Electron*., vol. 26, no. 1, pp. 210-222, Jan. 2011.

[12] L. Shang and J. Hu, "Sliding-mode-based direct power control of grid-connected wind-turbine-driven doubly fed induction generators under unbalanced grid voltage conditions," *IEEE Trans. Energy Convers*., vol. 27, no. 2, pp. 362–373, Jun. 2012.

[13] J. Rodriguez et al., "State of the art of finite control set model predictive control in power electronics," *IEEE Trans. Ind. Informat*., vol. 9, no. 2, pp. 1003–1016, May 2013.

[14] S. Vazquez, J. Rodriguez, M. Rivera, L. G. Franquelo, and M. Norambuena, "Model predictive control for power converters and drives: Advances and trends," *IEEE Trans. Ind. Electron*., vol. 64, no. 2, pp. 935–947, Feb. 2017.

[15] Y. Gui, C. Kim, C. C. Chung, J. M. Guerrero, Y. Guan, and J. C. Vasquez, "Improved direct power control for grid-connected voltage source converters," *IEEE Trans. Ind. Electron.*, vol. 65, no. 10, Oct. 2018.

[16] Y. Gui, C. Kim, C. C. Chung, "Grid voltage modulated direct power control for grid connected voltage source inverters," in *American Control Conf.,* Seattle, USA, 2017, pp. 2078-2084.

[17] S. Gao, H. Zhao, Y. Gui, "Dual grid voltage modulated direct power control of grid-connected voltage source converter under unbalanced network condition," in *IEEE PES ISGT-Asia*, Chengdu, China, 2019, pp. 2167-2172.

[18] S. Gao, H. Zhao, Y. Gui, *et al.*, "An improved direct power control for doubly fed induction generator," *IEEE Trans. Power Electron*., vol. 36, no. 4, pp. 4672-4685, Apr. 2021.

[19] S. Gao, H. Zhao, Y. Gui, *et al.*, "A novel direct power control for DFIG with parallel compensator under unbalanced grid condition," *IEEE Trans. Ind. Electron.*, vol. 68, no. 10, pp.9607-9618, Sep. 2020.

[20] Y. W. Li and C. Kao, "An accurate power control strategy for power-electronics-interfaced distributed generation units operating in a low-voltage multibus microgrid," *IEEE Trans. Power Electron*., vol. 24, no. 12, pp. 2977–2988, Dec. 2009.

[21] B. Li and L. Zhou, "Power decoupling method based on the diagonal compensating matrix for VSG-controlled parallel inverters in the microgrid," *Energies*, vol. 10, no. 12, pp. 2159–2171, 2017.

[22] K. De Brabandere, B. Bolsens, J. Van den Keybus, A. Woyte, J. Driesen, and R. Belmans, "A voltage and frequency droop control method for parallel inverters," *IEEE Trans. Power Electron*., vol. 22, no. 4, pp.1107–1115, Jul. 2007.

[23] Y. Li and Y. W. Li, "Power management of inverter interfaced autonomous microgrid based on virtual frequency-voltage frame," *IEEE Trans. Smart Grid*, vol. 2, no. 1, pp. 30–40, Mar. 2011.

[24] T. Wen, X. Zou, D. Zhu, *et al*, "Comprehensive perspective on virtual inductor or improved power decoupling of virtual synchronous generator control," *IET Renew. Power Gener*, vol. 14, no. 4, pp. 1-10, Dec. 2019.

[25] H. Mahmood, D. Michaelson, and J. Jiang, "Accurate reactive power sharing in an islanded microgrid using adaptive virtual impedances," *IEEE Trans. Power Electron*., vol. 30, no. 3, pp. 1605–1617, Mar. 2015.

[26] D. B. Rathnayake and B. Bahrani, "Multivariable Control Design for Grid-forming Inverters with Decoupled Active and Reactive Power Loops," *IEEE Trans. Power Electron*, 2022, doi: 10.1109/TPEL.2022.3213692.

[27] Y. Hu, Y. Shao, R. Yang, X. Long, and G. Chen, "A configurable virtual impedance method for grid-connected virtual synchronous generator to improve the quality of output current," *IEEE J. Emerg. Sel. Topics Power Electron*., May 22, 2019.

[28] T. Wu, Z. Liu, J. Liu, S. Wang and Z. You, "A Unified Virtual Power Decoupling Method for Droop-Controlled Parallel Inverters in

Microgrids," *IEEE Trans Power Electron*, vol. 31, no. 8, pp. 5587-5603, Aug. 2016.

[29] T. Wen, D. Zhu, X. Zou, B. Jiang, L. Peng and Y. Kang, "Power Coupling Mechanism Analysis and Improved Decoupling Control for Virtual Synchronous Generator," *IEEE Trans Power Electron*, vol. 36, no. 3, pp. 3028-3041, March 2021.

[30] S. Gao, H. Zhao, Y. Gui, J. Luo and F. Blaabjerg, "Impedance Analysis of Voltage Source Converter Using Direct Power Control," in *IEEE Trans. Energy Convers.*, vol. 36, no. 2, pp. 831-840, Jun. 2021

[31] Z. Peng, J. Wang, D. Bi, Y. Wen, Y. Dai, X. Yin, and J. Shen, "Droop control strategy incorporating coupling compensation and virtual impedance for microgrid application," *IEEE Trans. Energy Convers*., vol. 34, no. 1, pp. 277–291, Mar. 2019.

[32] Z. Gong, C. Liu, L. Shang, Q. Lai and Y. Terriche, "Power Decoupling Strategy for Voltage Modulated Direct Power Control of Voltage Source Inverters Connected to Weak Grids," *IEEE Trans. Sustain Energy*, 2022, doi: 10.1109/TSTE.2022.3204405.

[33] S. Gao, H. Zhao, Y. Gui, *et al.*, "A novel direct power control for DFIG with parallel compensator under unbalanced grid condition," *IEEE Trans. Industrial Electron.*, vol. 68, no. 10, pp. 9607-9618, Oct. 2021.

[34] Y. Komatsu and T. Kawabata, "A control method of active power filter where system voltage contains negative-phase-sequence component or zero-phase-sequence component," in *Proc. Int Power Electron. Drive Syst. Conf.*, 1995, pp. 583–586.

[35] Y. Suh and T. A. Lipo, "Modeling and analysis of instantaneous active and reactive power for pwm ac/dc converter under generalized unbalanced network," *IEEE Trans. Power Del.*, vol. 21, no. 3, pp. 1530–1540, Jul. 2006.

[36] Y. Zhang, J. Gao, and C. Qu, "Relationship between two direct power control methods for PWM rectifiers under unbalanced network," *IEEE Trans. Power Electron.*, vol. 32, no. 5, pp. 4084–4094, May 2017.

[37] Y. Zhang, J. Gao, and D. Xu, "Direct power control of doubly fed induction generator using extended power theory under unbalanced network", *IEEE Trans. Power Electron.*, vol. 34, no. 12, pp. 12024-12037, March, 2019.

[38] K. De Brabandere, B. Bolsens, J. Van den Keybus, *et al.*, "A voltage and frequency droop control method for parallel inverters," *IEEE Trans. Power Electron*., vol. 22, no. 4, pp.1107–1115, Jul. 2007.

[39] J. Svensson, M. Bongiorno, A. Sannino, "Practical implementation of delayed signal cancellation method for phase-sequence separation," *IEEE Trans. Power Deliv.*, vol. 22, no. 1, pp. 18-26, Jan. 2007.

[40] G. Abad, M. A. Rodriguez, G. Iwanski, and J. Poza, "Direct power control of doubly-fed-induction-generator-based wind turbines under unbalanced grid voltage," *IEEE Trans. Power Electron*., vol. 25, no. 2, pp. 442–452, Feb. 2010.

[41] Q. Huang and K. Rajashekara, "An improved delayed signal cancellation PLL for fast grid synchronization under distorted and unbalanced grid condition," *IEEE Trans. Ind. Appl.*, vol. 53, no. 5, pp. 4985–4997, Sep. 2017.

[42] L. Asiminoaei, R. Teodorescu, F. Blaabjerg, *et al*., "Implementation and test of an online embedded grid impedance estimation technique for PV inverters," *IEEE Trans Industrial Electron*., vol. 52, no. 4, pp. 1136-1144, 2005.

[43] J. Yang, W. Li, T. Chen, *et al*., "Online estimation and application of power grid impedance matrices based on synchronized phasor measurements," *IET Gener. Transm. Distrib*., vol. 4, no. 9, pp. 1052-1059, 2010.

[44] M. Ghorbal, W. Ghzaiel, *et al.*, "Online detection and estimation of grid impedance variation for distributed power generation," in 16th IEEE Mediterranean Electrotechnical Conf., Yasmine Hammamet, Tunisia, 2012, pp. 555-560.

[45] T. Zheng, L. Chen, Y. Guo, *et al*. "Comprehensive control strategy of virtual synchronous generator under unbalanced voltage conditions," *IET Gener. Transm. Distrib.,* vol. 12, no. 7, pp. 1621-1630, 2017.

[46] D. Yang, X. Wang, F. Liu, K. Xin, Y. Liu, and F. Blaabjerg, "Adaptive reactive power control of PV power plants for improved power transfer capability under ultra-weak grid conditions," *IEEE Trans. Smart Grid*, vol. 10, no. 2, pp. 1269–1279, Mar. 2019.